Supporting Information for "How to design an icosahedral quasicrystal through directional bonding"

Eva G. Noya,[1] Chak Kui Wong,[2] Pablo Llombart,[1] and Jonathan P. K. Doye[2]

[1)] *Instituto de Química Física Rocasolano, Consejo Superior de Investigaciones Científicas, CSIC, Calle Serrano 119, 28006 Madrid, Spain*

[2)] *Physical and Theoretical Chemistry Laboratory, Department of Chemistry, University of Oxford, South Parks Road, Oxford, OX1 3QZ, United Kingdom*

(Dated: 2 February 2021)

S1. QUASICRYSTAL ENVIRONMENT ANALYSIS

As a first step in generating patchy particle designs, we analysed the local environments in the ideal quasicrystals, as outlined in Section B of the Methods. For the ideal BCI QC, the eleven environments with coordination number greater than or equal to two were represented in Fig. 1. In Table S1 we list all the environments along with the proportions with which they appear in the ideal QC. All of the environments are explicitly represented by a patchy particle type in the BCI 5P model, except for the environments with a coordination number of 0 or 1.

The environments in the ideal PI QC are given in Table S2. In this case, as we found that a patchy particle model that represented just the three environments in the icosahedral cluster in Fig. 3a was already able to assemble into a QC, we did not consider more complex models that attempted to represent more of the environments in the ideal QC. Particles in these three local environments only represent 49% of the total number in the ideal QC.

Index	n_{neigh}	Angles	Mole fraction	Particle type
1	0		0.013	
2	1		0.015	
3	2	116.57	0.019	B
4	3	116.57×3	0.096	B
5	4	116.57 ×3, 100.81×3	0.427	B
6	4	116.57×5, 63.43	0.154	Y
7	4	138.18, 116.57, 100.81×4	0.057	P
8	5	138.18, 116.57, 110.91×2, 100.81×4, 58.28×2	0.065	P
9	5	148.28, 116.57×3, 110.91, 100.81×3, 58.28×2	0.083	G
10	5	116.57×7, 63.43×3	0.011	R
11	6	116.57×10, 63.43×5	0.016	R
12	6	148.28×2, 116.57×3, 110.91×2, 108.0 , 100.81×3, 58.28×4	0.015	G
13	7	148.28×3, 116.57×3, 110.91×3, 108.0×3, 100.81×3, 58.28×6	0.028	G

TABLE S1. Local environments in the ideal BCI QC. The number of nearest neighbours is defined as the number of particles within a distance of $1.4\,\sigma$ (this cutoff provides a clear distinction between first and second coordination shells, see Extended Data Fig. 6). The angles formed between a particle and its pairs of nearest neighbours are provided in the third column. The proportion with which each local environment appears in the ideal BCI QC is given in the fourth column. The last column gives the patchy particle type by which we represent an environment in the BCI 5P model (B: blue; Y: yellow; P: purple; R: red; G: green).

Index	n_{neigh}	Angles	Mole fraction	Particle type
1	4	138.18×3, 70.53×3	0.0197	
2	5	138.18×5, 70.53×5	0.2840	G
3	5	138.19×3, 125.26×2, 70.53×3, 69.09×2	0.0194	
4	6	138.18×4, 125.26×3, 109.47, 70.53×5, 69.09×2	0.0833	
5	6	138.18×6, 109.47×2, 70.53×7	0.3041	
6	6	138.18×3, 125.26×4, 108.00, 70.53×3, 69.09×4	0.0187	R
7	7	138.18×5, 125.26×4, 109.47×2, 70.53×8, 69.09×2	0.0486	
8	7	138.18×7, 109.47×4, 108.00, 70.53×10	0.0174	
9	7	138.18×3, 125.26×6, 108.00×3, 70.53×3, 69.09×6	0.0278	R
10	8	138.18×9, 109.47×6, 70.53×12, 41.81	0.1569	B
11	10	138.18×12, 109.47×12, 70.53×24, 41.81×3	0.0148	
12	12	180.00×2, 138.18×15, 109.47×11, 70.53×24, 41.81×7	0.0024	
13	15	180.00×5, 138.18×20, 109.47×30, 70.53×35, 41.81×15	0.0018	
14	20	180.00×10, 138.18×30, 109.47×60, 70.53×60, 41.81×30	0.0009	

TABLE S2. Local environments in the PI QC. The number of nearest neighbours is defined as the number of particles with a distance of $1.2\,\sigma$ (i.e., up to the second peak in the PDF, see Extended Data Fig. 7). The angle formed between a particle and all its pairs of nearest neighbours are provided in the third column. The proportion with which each local environment appears in the ideal PI QC is given in the fourth column. The last column gives the patchy particle type by which we represent an environment in the PI 3P model (G: green; R: red; B: blue). Note that in the PI 3P model we only represent those environments that are part of the icosahedral cluster in Fig. 3a, and do not introduce particle types for the new environments that appear in the matrix between these clusters (represented as yellow (environment 5) and pink in Extended Data Fig. 3). We also do not attempt to represent the high coordination particles that occupy positions at the centre of the icosahedral clusters (environments 12–14).

S2. PARTICLE DESIGNS

The details of the patchy particle properties for all the model designs are given in Tables S3 to S8. The particles have point group symmetries that are subgroups of the I_h point group, and when the particles are appropriately oriented (e.g. so that the particle's symmetry elements are aligned with I_h), their patch vectors are only directed along the 2-, 3- and 5-fold axes of symmetry for the BCI examples, and the 2- and 3-fold axes for the PI examples, as illustrated in Extended Data Fig. 8e and f. The angles associated with the environments in Tables S1 and S2, thus, all correspond to angles between different symmetry axes of I_h.

The preferred torsional angles ensure that when a patch-patch bond is formed the patches of both particles can point along the symmetry axes of I_h. Thus, the torsional constraints encourage the propagation of long orientational order consistent with the I_h point group or a subgroup thereof. Note that the allowed offset angles might only represent a subset of those that would ensure propagation of the orientational order, because these are the only ones that are associated with the environments in the ideal quasicrystals and thus encode certain structural preferences. For example, the torsional offset angles for patch 1 of the blue particles (which align along 5-fold axes) represent only two of the five potential angles consistent with icosahedral orientational order (the other three would be $\pm 36°$ and $180°$). Similarly, patches 4–6 of the red particles of PI 3P, which align along 2-fold axes, only have a single preferred torsional angle of $0°$ (rather than also $180°$) as only the former is consistent with the red particles forming dodecahedral clusters.

Note that some patches in the BCI 5P, BCI 3P and BCI 2P (namely (some of) those associated with the blue particles) models can bond with patches on multiple particle types. This multiplicity gives a potential source of configurational entropy that may help to stabilize the quasicrystal, in addition to the configurational entropy associated with the different ways of arranging the dangling bonds. However, as illustrated by the BCI 2P-mod and all the PI systems this is not a necessary feature to observe IQC formation.

Particle type	Patch index	Patch vector	Reference vector patch	Offset angle	Specificity
Blue (B)	P_B^1	(-0.850651,0.525731,0.0)	P_B^4	±108.0	P_B^{1-3},$P_Y^{1,3}$ (1.0), P_R^1 (1.2)
C_{3v}	P_B^2	(0.525731,0.0,-0.850651)	P_B^4	±108.0	P_B^{1-3},$P_Y^{1,3}$ (1.0), P_R^1 (1.2)
196/284	P_B^3	(0.0,-0.850651,0.525731)	P_B^4	±108.0	P_B^{1-3},$P_Y^{1,3}$ (1.0), P_R^1 (1.2)
	P_B^4	(0.577350,0.577350,0.577350)	P_B^1	±60.0 180.0	P_B^4,$P_P^{4,5}$(1.0), P_G^7(1.2)
Yellow (Y)	P_Y^1	(-0.525731,0.0,-0.850651)	–	–	P_B^{1-3} (1.0)
C_{2v}	P_Y^2	(0.850651,-0.525731,0.0)	P_Y^4	0.0	$P_P^{1,2}$ (1.0)
12/284	P_Y^3	(-0.525731,0.0,0.850651)	–	–	P_B^{1-3} (1.0)
	P_Y^4	(0.850651,0.525731,0.0)	P_Y^2	0.0	$P_P^{1,2}$ (1.0)
Purple (P)	P_P^1	(-0.850651,0.525731,0.0)	P_P^2	0.0	$P_Y^{2,4}$ (1.0)
C_{2v}	P_P^2	(0.850651,0.525731,0.0)	P_P^1	0.0	$P_Y^{2,4}$ (1.0)
12/284	P_P^3	(0.0,1.0,0.0)	P_P^2	0.0, 180.0	P_P^3 (1.0)
	P_P^4	(0.0,-0.356822,-0.934172)	P_P^5	±60.0, 180.0	P_B^4 (1.0)
	P_P^5	(0.0,-0.356822,0.934172)	P_P^4	±60.0, 180.0	P_B^4 (1.0)
Red (R)	P_R^1	(-0.525731, 0.0, -0.850651)	–	–	P_B^{1-3} (1.2)
C_{5v}	P_R^2	(0.850651, -0.525731, 0.0)	P_R^1	0.0	$P_G^{1,2,4}$ (0.7)
24/284	P_R^3	(-0.525731, 0.0, 0.850651)	P_R^1	0.0	$P_G^{1,2,4}$ (0.7)
	P_R^4	(0.0, -0.850651, 0.525731)	P_R^1	0.0	$P_G^{1,2,4}$ (0.7)
	P_R^5	(0.850651, 0.525731, 0.0)	P_R^1	0.0	$P_G^{1,2,4}$ (0.7)
	P_R^6	(0.0, 0.850651, 0.525731)	P_R^1	0.0	$P_G^{1,2,4}$ (0.7)
Green (G)	P_G^1	(-0.850651, 0.525731, 0.0)	P_G^7	0.0	P_R^{2-6} (0.7)
C_{3v}	P_G^2	(0.0, -0.850651, 0.525731)	P_G^7	0.0	P_R^{2-6} (0.7)
40/284	P_G^3	(-0.809017, -0.309017, 0.50)	P_G^7	0.0	$P_G^{3,5,6}$ (0.7)
	P_G^4	(0.850651, 0.525731, 0.0)	P_G^7	0.0	P_R^{2-6} (0.7)
	P_G^5	(0.0, 1.0, 0.0)	P_G^7	0.0	$P_G^{3,5,6}$ (0.7)
	P_G^6	(0.809017, -0.309017, 0.50)	P_G^7	0.0	$P_G^{3,5,6}$ (0.7)
	P_G^7	(0.0, -0.356822, -0.934172)	P_G^1	±60.0, 180.0	P_B^4 (1.2)

TABLE S3. Description of the geometry and specificity of the particle types of the BCI 5P model. For each particle type, the positions of the patches on the particle surface are specified by the patch unit vectors. For each patch, the reference patch and offset angles used for evaluating the torsional interactions are provided. The specificity of each patch, along with the interaction strength parameter $\varepsilon_{\alpha\beta}$ in parentheses, are given in the last column. To simplify the implementation of the model, torsional contributions are not imposed on the blue-yellow and blue-red interactions. The strength of the green-red and green-green interactions are reduced to 0.7 so that the assembly of the triacontahedral clusters occurs in a similar temperature window as the assembly of the remaining particles. Blue-green and blue-red interactions were enhanced to 1.2 to disfavour the phase separation of blue particles.

Particle type	Patch index	Patch vector	Reference patch	Offset angle	Specificity
Blue (B)	P_B^1	(-0.850651, 0.525731, 0.0)	P_B^4	±108.0	P_B^{1-3} (1.0), P_R^1 (1.2)
C_{3v}	P_B^2	(0.525731, 0.0, -0.850651)	P_B^4	±108.0	P_B^{1-3} (1.0), P_R^1 (1.2)
	P_B^3	(0.0, -0.850651, 0.525731)	P_B^4	±108.0	P_B^{1-3} (1.0), P_R^1 (1.2)
	P_B^4	(0.577350, 0.577350, 0.577350)	P_B^1	±60.0 180.0	P_B^4(1.0), P_G^4(1.2)
Red (R)	P_R^1	(-0.525731, 0.0, -0.850651)	–	–	P_B^{1-3} (1.2)
C_{5v}	P_R^2	(0.850651, -0.525731, 0.0)	–	–	P_G^{1-3} (0.92)
	P_R^3	(-0.525731, 0.0, 0.850651)	–	–	P_G^{1-3} (0.92)
	P_R^4	(0.0, -0.850651, 0.525731)	–	–	P_G^{1-3} (0.92)
	P_R^5	(0.850651, 0.525731, 0.0)	–	–	P_G^{1-3} (0.92)
	P_R^6	(0.0, 0.850651, 0.525731)	–	–	P_G^{1-3} (0.92)
Green (G)	P_G^1	(-0.850651, 0.525731, 0.0)	–	–	P_R^{2-6} (0.92)
C_{3v}	P_G^2	(0.0, -0.850651, 0.525731)	–	–	P_R^{2-6} (0.92)
	P_G^3	(0.850651, 0.525731, 0.0)	–	–	P_R^{2-6} (0.92)
	P_G^4	(0.0, -0.356822, -0.934172)	P_G^1	±60.0, 180.0	P_B^4 (1.2)

TABLE S4. Description of the geometry and specificity of the particle types of the BCI 3P model. For each particle type, the positions of the patches on the particle surface are specified by the patch unit vectors. For each patch, the reference patch and offset angles used for evaluating the torsional interactions are provided. The specificity of each patch, along with the interaction strength parameter $\varepsilon_{\alpha\beta}$ in parentheses, are given in the last column. In this model, torsional angles are only imposed for blue-blue and blue-green interactions. The strength of the red-green interactions are increased compared to the BCI 5P system, as the triacontahedra are now stabilized by fewer bonds.

Particle type	Patch index	Patch vector	Reference patch	Offset angle	Specificity
Blue (B)	P_B^1	(-0.850651, 0.525731, 0.0)	P_B^4	±108.0	P_B^{1-3} (1.0)
C_{3v}	P_B^2	(0.525731, 0.0, -0.850651)	P_B^4	±108.0	P_B^{1-3} (1.0)
	P_B^3	(0.0, -0.850651, 0.525731)	P_B^4	±108.0	P_B^{1-3} (1.0)
	P_B^4	(0.577350, 0.577350, 0.577350)	P_B^1	±60.0, 180.0	P_B^4 (1.0), P_G^4(1.15)
Green (G)	P_G^1	(-0.809017, -0.309017, 0.50)	P_G^4	0.0	P_G^{1-3} (1.0)
C_{3v}	P_G^2	(0.0, 1.0, 0.0)	P_G^4	0.0	P_G^{1-3} (1.0)
	P_G^3	(0.809017, -0.309017, 0.50)	P_G^4	0.0	P_G^{1-3} (1.0)
	P_G^4	(0.0, -0.356822, -0.934172)	P_G^5	±60.0, 180.0	P_B^4 (1.15)
	P_G^5	(-0.850651, 0.525731, 0.0)	–	–	–

TABLE S5. Description of the geometry and specificity of the particle types of the BCI 2P model. For each particle type, the positions of the patches on the particle surface are specified by the patch unit vectors. For each patch, the reference patch and offset angles used for evaluating the torsional interactions are provided. The specificity of each patch, along with the interaction strength $\varepsilon_{\alpha\beta}$ in parentheses, are given in the last column. Patch 5 of the green particles P_G^5 is a non-interacting patch that was used only as a reference vector for calculating the torsional angles associated with bonds formed by patch P_G^4.

Particle type	Patch index	Patch vector	Reference patch	Offset angle	Specificity
Green (G)	P_G^1	(-0.577350, -0.577350, -0.577350)	P_G^3	0.0,-168.5	P_B^{3-8} (1.0)
C_{5v}	P_G^2	(-0.577350, -0.577350, 0.577350)	P_G^1	0.0,-168.5	P_B^{3-8} (1.0)
	P_G^3	(0.0, 0.356820, -0.934173)	P_G^5	0.0,-168.5	P_B^{3-8} (1.0)
	P_G^4	(0.0, 0.356817, 0.934174)	P_G^2	0.0,-168.5	P_B^{3-8} (1.0)
	P_G^5	(0.356817, 0.934174, 0.0)	P_G^4	0.0,-168.5	P_B^{3-8} (1.0)
Red (R)	P_R^1	(-0.356817, -0.934174, 0.0)	P_R^7	0.0	$P_B^{1,2}$ (1.0)
C_{3v}	P_R^2	(0.0, -0.356817, -0.934174)	P_R^7	0.0	$P_B^{1,2}$ (1.0)
	P_R^3	(-0.934174, 0.0, -0.356817)	P_R^7	0.0	$P_B^{1,2}$ (1.0)
	P_R^4	(0.309023, -0.5, 0.809018)	P_R^7	0.0	P_R^{4-6} (1.0)
	P_R^5	(-0.5, 0.809018, 0.309023)	P_R^7	0.0	P_R^{4-6} (1.0)
	P_R^6	(0.809018, 0.309023, -0.5)	P_R^7	0.0	P_R^{4-6} (1.0)
	P_R^7	(0.577350, 0.577350,0.577350)	—	—	—
Blue (B)	P_B^1	(-0.577350, -0.577350, -0.577350)	P_B^2	0.0	P_R^{1-3} (1.0)
C_{2v}	P_B^2	(-0.356817, -0.934174, 0.0)	P_B^1	0.0	P_R^{1-3} (1.0)
	P_B^3	(0.577350, -0.577350, -0.577350)	—	—	P_G^{1-5} (1.0)
	P_B^4	(-0.934173, 0.0, 0.356820)	—	—	P_G^{1-5} (1.0)
	P_B^5	(0.577350, 0.577350, -0.577350)	P_B^1	0.0,-168.5	P_G^{1-5} (1.0)
	P_B^6	(0.934174, 0.0, 0.356817)	P_B^2	0.0,-168.5	P_G^{1-5} (1.0)
	P_B^7	(-0.356820, 0.934173, 0.0)	P_B^1	0.0,-168.5	P_G^{1-5} (1.0)
	P_B^8	(0.0, 0.356820, 0.934173)	P_B^2	0.0,-168.5	P_G^{1-5} (1.0)

TABLE S6. Description of the geometry and specificity of the particle types of the PI 3P WT model. For each particle type, the positions of the patches on the particle surface are specified by the patch unit vectors. For each patch, the reference patch and offset angles used for evaluating the torsional interactions are provided. The specificity of each patch, along with the interaction strength parameter $\varepsilon_{\alpha\beta}$ in parentheses, are given in the last column. Patch 7 on the red particles P_R^7 is a non-interacting patch that was used only as the reference vector for calculating the torsional angles associated with bonds formed by the remaining six patches on red particles P_R^{1-6}. The $\sigma_{LJ,R-R}$ parameter for the red-red interactions was set to $0.7\sigma_{LJ}$ (where σ_{LJ} is the value used for all other interactions and that was taken as the distance unit) to take into account that the distance between red-red particles is about 0.7 smaller than the remaining interparticle distances in the target ideal primitive IQC. To simplify the implementation of the model, torsional contributions to the bonds formed by patches P_B^3 and P_B^4 are not imposed. Simulations using this model with all torsional contributions removed (PI 3P NT) also assemble into an IQC.

Particle type	Patch index	Patch vector	Reference patch	Offset angle	Specificity
Green (G)	P_G^1	(-0.577350, -0.577350, -0.577350)	P_G^3	0.0,-168.5	P_B^{1-6} (1.0)
C_{5v}	P_G^2	(-0.577350, -0.577350, 0.577350)	P_G^1	0.0,-168.5	P_B^{1-6} (1.0)
	P_G^3	(0.0, 0.356820, -0.934173)	P_G^5	0.0,-168.5	P_B^{1-6} (1.0)
	P_G^4	(0.0, 0.356817, 0.934174)	P_G^2	0.0,-168.5	P_B^{1-6} (1.0)
	P_G^5	(0.356817, 0.934174, 0.0)	P_G^4	0.0,-168.5	P_B^{1-6} (1.0)
Blue (B)	P_B^1	(0.577350, -0.577350, -0.577350)	—	—	P_G^{1-5} (1.0)
C_{2v}	P_B^2	(-0.934173, 0.0, 0.356820)	—	—	P_G^{1-5} (1.0)
	P_B^3	(0.577350, 0.577350, -0.577350)	P_B^1	0.0,-168.5	P_G^{1-5} (1.0)
	P_B^4	(0.934174, 0.0, 0.356817)	P_B^2	0.0,-168.5	P_G^{1-5} (1.0)
	P_B^5	(-0.356820, 0.934173, 0.0)	P_B^1	0.0,-168.5	P_G^{1-5} (1.0)
	P_B^6	(0.0, 0.356820, 0. 934173)	P_B^2	0.0,-168.5	P_G^{1-5} (1.0)

TABLE S7. Description of the geometry and specificity of the particle types of the PI 2P WT model. For each particle type, the positions of the patches on the particle surface are specified by the patch unit vectors. For each patch, the reference patch and offset angles used for evaluating the torsional interactions are provided. The specificity of each patch, along with the interaction strength parameter $\varepsilon_{\alpha\beta}$ in parentheses, are given in the last column. Note that the two patches on the blue particles that only interact with red particles in the 3P model are no longer needed, so that now the blue particles have only six patches, instead of eight. To simplify the implementation of the model, torsional contributions to the bonds formed by patches P_B^1 and P_B^2 are not imposed. Simulations using this model with all torsion contributions removed (PI 2P NT) also assemble into an IQC.

Particle type	Patch index	Patch vector	Reference patch	Offset angle	Specificity
Blue (B)	P_B^1	(-0.850651, 0.525731, 0.0)	P_B^4	0.0,±108.0	P_B^{1-3} (1.0)
C_{3v}	P_B^2	(0.525731, 0.0, -0.850651)	P_B^4	0.0,±108.0	P_B^{1-3} (1.0)
	P_B^3	(0.0, -0.850651, 0.525731)	P_B^4	0.0,±108.0	P_B^{1-3} (1.0)
	P_B^4	(0.577350, 0.577350, 0.577350)	P_B^1	±60.0, 180.0	P_G^4(1.15)
Green (G)	P_G^1	(-0.809017, -0.309017, 0.50)	P_G^4	0.0	P_G^{1-3} (1.0)
C_{3v}	P_G^2	(0.0, 1.0, 0.0)	P_G^4	0.0	P_G^{1-3} (1.0)
	P_G^3	(0.809017, -0.309017, 0.50)	P_G^4	0.0	P_G^{1-3} (1.0)
	P_G^4	(0.0, -0.356822, -0.934172)	P_G^5	±60.0, 180.0	P_B^4 (1.15)
	P_G^5	(-0.850651, 0.525731, 0.0)	–	–	–

TABLE S8. Description of the geometry and specificity of the particle types of the BCI 2P-mod system that is a modification to the BCI 2P model in order to allow realization using DNA origami. For each particle type, the positions of the patches on the particle surface are specified by the patch unit vectors. For each patch, the reference patch and offset angles used for evaluating the torsional interactions are provided. The specificity of each patch, along with the interaction strength $\varepsilon_{\alpha\beta}$ in parenthesis, are given in the last column. Patch 5 of the green particles P_G^5 is a non-interacting patch that was used only as a reference vector for calculating the torsional angles associated with bonds formed by patch P_G^4. The modifications were to allow three equivalent offset angles for patches P_B^{1-3} and to not allow patch P_B^4 to interact with copies of itself. The structural effects of these modifications are illustrated in Fig. S1.

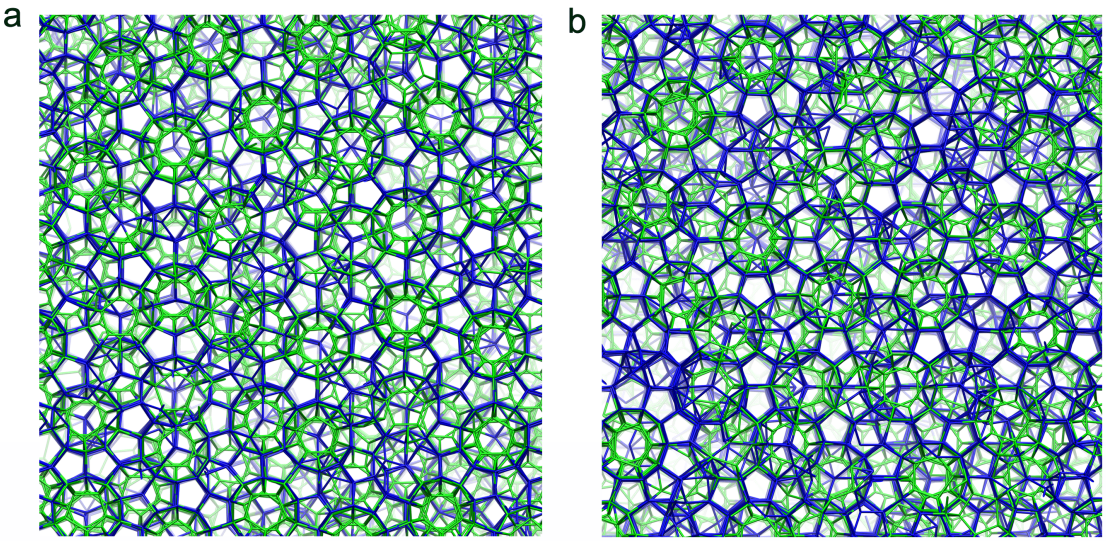

FIG. S1. Projection of the **a** BCI 2P-mod and **b** BCI 2P models along the five-fold axis. The distance between the dodecahedra is appreciably shorter in the BCI 2P-mod system. Blue and green particles are in similar proportion in the BCI 2P-mod model, whereas blue particles are more abundant in the BCI 2P model (about 60%). Blue-blue bonds are directed always along the five-fold axes in the BCI 2P-mod system, whereas in the original BCI 2P model blue-blue bonds (associated with patch 4) can also be directed along the three-fold axes.

System	$T^*_{\rm nuc}$	$T^*_{\rm growth}$	$N_{\rm final}$	Composition
BCI 5P	0.087	0.090	70 000	0.72 B, 0.009 Y, 0.013 P, 0.10 R, 0.16 G
BCI 3P	0.087	0.088	53 500	0.72 B, 0.11 R, 0.17 G
BCI 2P	0.086	0.089	77 500	0.57 B, 0.43 G
BCI 2P-mod	0.089	0.092	48 200	0.52 B, 0.48 G
PI 3P WT	0.114	0.125	66 000	0.45 G, 0.16 R, 0.39 B
PI 3P NT	0.118	0.128	66 000	0.45 G, 0.16 R, 0.39 B
PI 2P WT	0.110	0.115	70 500	0.54 G, 0.46 B
PI 2P NT	0.113	0.118	67 500	0.54 G, 0.46 B

TABLE S9. Details of the main simulations used for each system. $T^*_{\rm nuc}$ is the temperature used for the initial nucleation of a solid cluster. $T^*_{\rm growth}$ is the temperature used for the growth of that nucleus into a large assembly. $N_{\rm final}$ is the approximate final size of the solid cluster. The composition of a cluster of size $N_{\rm final}$ is given in the last column. The structural and dynamic analysis of the resulting IQCs was performed at $T^*_{\rm growth}$.

S3. FURTHER RESULTS

A. Effects of temperature

For the nucleation stage of our simulation the temperature was chosen to be as high as possible consistent with nucleation on reasonable simulation time scales. This choice makes it likelier that only a single cluster will nucleate. For the BCI 5P system, the estimates of the melting point in Section S4 suggest this temperature probably corresponds to a supercooling in the range 10-20%.

For the growth stage of our simulations the temperature was increased slightly, the aim being to use a temperature as high as possible consistent with reasonable growth rates on the simulation time scales. This choice ensures a high degree of order in the growing clusters, as well as preventing nucleation of further clusters. Preliminary simulations at lower temperatures typically led to more defective quasicrystals with less sharp diffraction patterns. Note that as our simulations were in the NVT ensemble, the concentration of particles in the fluid phase decreases as the cluster grows. At the end of our simulations, although the clusters were still growing, typically the growth rate had become extremely slow because of the low density of particles in the fluid. At longer times we would expect the growth to stop when equilibrium between the solid cluster and the fluid had been reached.

The specific temperatures used in the nucleation and growth stages of our main simulations are given in Table S9 for all systems.

The dynamic properties of the quasicrystals are likely to be particularly sensitive to temperature. To illustrate this, we also evaluated the van Hove autocorrelation function for the BCI 5P system at a higher temperature than reported in Extended Data Fig. 9, namely at $T^* = 0.096$ rather than 0.090. As expected, the mobility of the particles is higher at higher temperature, but with the difference in mobility between the blue matrix particles and the red and green particles that form the triacontahedral clusters still very pronounced (Fig. S2).

B. Effects of composition

In the results reported in the main text, when choosing the initial composition of the fluid the aim was to match the preferred composition of the quasicrystal. In this way, the composition of the fluid in our NVT simulations remains roughly constant as the quasicrystalline cluster grows.

The compositions of the final clusters are given in Table S9. Some features are easy to rationalize. For example, in the PI 2P systems, the patches on the blue particles can only interact with the patches on the green particles and vice versa. Full bonding could only potentially therefore happen when the number of blue patches and green patches in the system is equal. This occurs when the mole fraction of green particles is $6/(6+5) = 0.545$; this is the composition observed in simulations. In the PI 3P systems, the ratio of blue to green particles is the same. For the BCI 5P, 3P and 2P systems, such arguments cannot be applied to the overall system as a number of patches have multiple interaction partners. However, the ratio of red to green particles would be expected to be 3:5 as is approximately observed. Finally, for the BCI 2P-mod system, the blue and green particles each have one patch that can interact with each other, thus suggesting an equimolar composition, as is close to being observed.

Here we also report the results of additional simulations with different compositions. Firstly, we were interested to see what would happen in simulations of one-component systems of some of our particles. We first considered a system of just blue BCI particles (with torsions). In particularly, we were interested whether they might form a

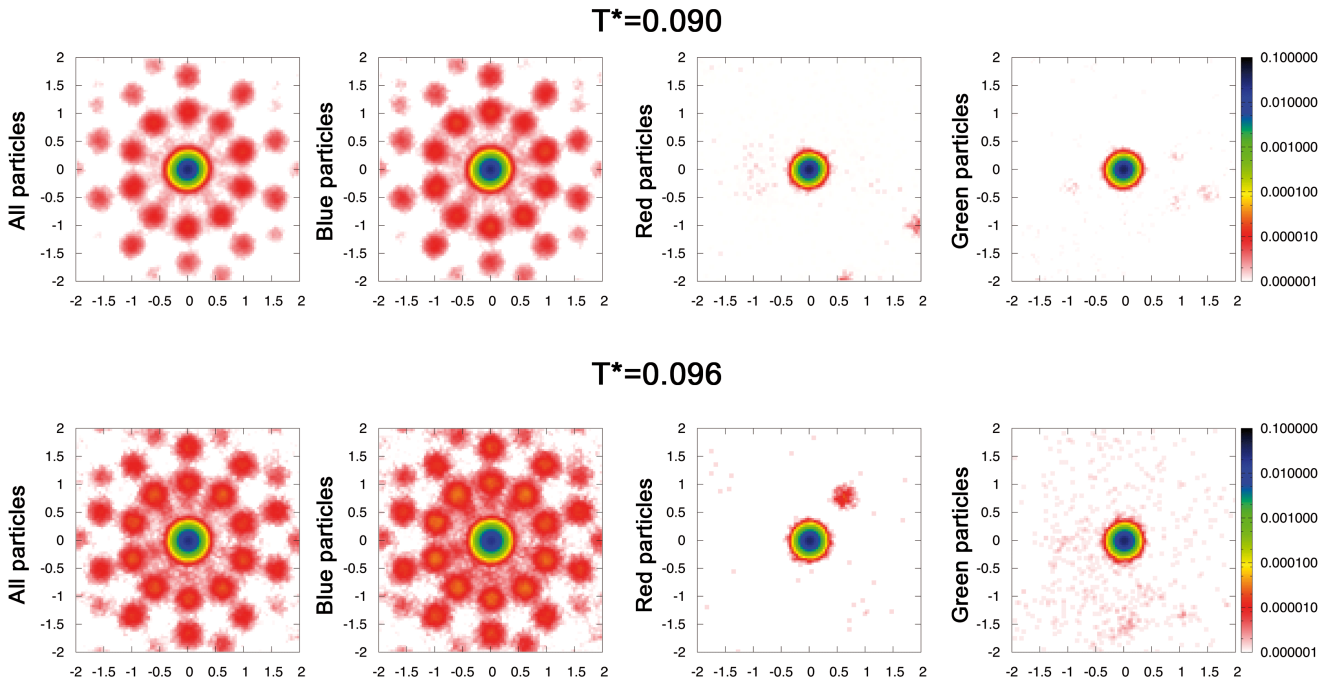

FIG. S2. Effect of temperature on the dynamics of the BCI 5P model. The van Hove autocorrelation function is shown for two different temperatures, T*=0.090 and T*=0.096. As expected, mobility is higher at higher temperatures, but the main features of the van Hove function are similar in both cases. The mobility of the green and red particles (that are often found forming triacontahedra) is much lower than that of the blue particles at both temperatures. Yellow and purple particles are incorporated to the IQC cluster in very low concentrations and for this reason data are not shown for these two particle types.

one-component quasicrystal or whether they would form a periodic crystal instead. The particles have C_{3v} symmetry with the relationship of the patch vectors to the icosahedral point group as illustrated in Extended Data Fig. 8e; i.e. when appropriately oriented, patch 4 points along a three-fold axis of I_h and patches 1–3 along five-fold axes. The torsional interactions ensure that global orientational order is maintained as a cluster of blue particles grows. The question then is whether the growth leads to the relevant patch vectors being equally likely to point along any of the three- and five-fold axes as in the IQC, or whether they only point along a subset associated with a subgroup of I_h.

Our simulations of this system always led to the nucleation and growth of cubic BC8 crystals (Fig. S3a). The BC8 crystals form as this allows the particles to be fully bonded, and are thus expected to be significantly lower in energy than potential competing IQCs. In the crystal, the patch 4 vectors only point along the four three-fold directions that are retained in the cubic subgroups of I_h (patches 1–3 are equally likely to point approximately along all six five-fold directions of I_h). Interestingly, the BC8 crystal has been suggested to be an approximant of a putative tetrahedral icosahedral quasicrystal.[1]

It is also noteworthy that the geometric properties of a patchy-particle model previously designed to form BC8 crystals are very similar to the blue particles,[2] the main difference being that distinct patchy particles were used for the two enantiomeric environments in the crystal, one with a preferred torsional offset angle of 108° for patches 1–3 and the other with −108°, whereas the BCI blue particles allow ±108°.

The second one-component system that we considered was of modified BCI 2P green particles. The three self-interacting patches of the green particles would just lead to the assembly of a fluid of dodecahedral clusters in the absence of other particles. We therefore modified patch 4 to allow it to interact with patch 4 on other green particles. The assemblies that resulted are shown in Fig. S3b. Again a cubic crystal resulted. It can be considered as a body-centred-cubic packing of dodecahedra. Each dodecahedra is directly bonded to the eight dodecahedra surrounding it by patch 4 bonds along the cubic three-fold directions. The crystal is not fully bonded, as not all patch 4's can be bonded.

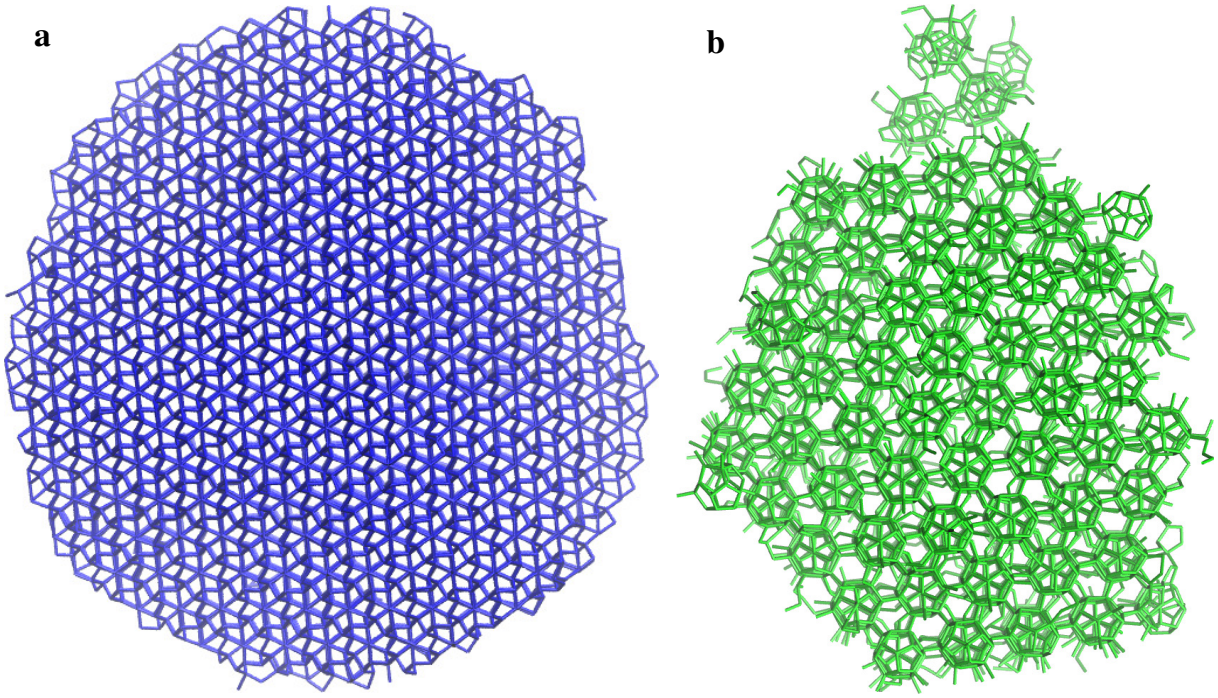

FIG. S3. **a**, A BC8 crystal grown from a fluid of pure blue BCI particles viewed along a three-fold axis. All particles are 4-coordinate. **b**, A cubic crystal grown from modified BCI 2P green particles viewed along a three-fold axis. The crystal is a body-centred cubic packing of dodecahedra. The particles are modified to allow patch 4 to interact with patch 4 on other green particles.

Secondly, we checked the sensitivity of IQC formation to the composition of the initial fluid mixture by performing additional simulations of the BCI 2P and PI 2P WT systems. In the case of the BCI 2P system we ran additional simulations with blue particle mole fractions of 0.3 and 0.83 (this compares to the preferred composition of 0.57). In both cases, IQCs still assembled, albeit at a slightly lower temperatures and with quasicrystal compositions that were closer to but different from the preferred composition, namely 0.45 and 0.62, respectively. For this system, the quasicrystal composition effectively controls the distance between the green dodecahedral clusters. As long as the proportion of clusters is still high enough to ensure that the blue matrix particles retain icosahedral orientational order (rather than adopting cubic BC8 order), quasicrystallinity is to be expected.

As a contrasting example, we also ran simulations of the PI 2P WT system with green particle mole fractions of 0.3 and 0.8, compared to a preferred composition of 0.54. Here, both the green and blue particles are part of the matrix. Again, IQCs still formed from these mixtures with the green particle mole fractions in the quasicrystals being 0.48 and 0.58, respectively. The reduced variation in the quasicrystal composition compared to the BCI 2P results was expected, given that there is no equivalent of the structural mechanism for varying the quasicrystal composition that is available to BCI 2P. Furthermore, the degree of incomplete bonding is expected to increase as the composition deviates further from the ideal value of $6/11 = 0.545$ that would potentially allow all patches to be bonded.

The above results confirm that IQC formation is robust to large changes in the fluid composition.

We should note that because the composition of the IQC in the above NVT simulations does not match the fluid, the composition of the fluid will change as the quasicrystal grows. This can lead to growth stopping if the fluid becomes too depleted in the minority species. Also, in the BCI 2P example with excess blue particles (the 0.83/0.17 blue/green mixture) there is potential competition with the BC8 crystal that can be formed purely from blue particles. The fluid first nucleated an IQC cluster, showing even at this composition IQC formation is preferred over phase separation; the greater strength of the blue-green interactions (Table S5) helps to discourage this phase separation. However, when the fluid was running out of green particles, grains of the BC8 crystal made of blue particles started to form on the cluster surface.

C. Effects of torsions

As was noted in the main text, the main BCI systems were not able to form quasicrystals without a torsional component to the potential. In all the BCI systems (except BCI 2P-mod) all the patches of the blue particles are able to self-interact. Therefore, to suppress any tendency to phase separate, and to favour the incorporation of the icosahedral clusters into the blue matrix, the strength of the blue-red and blue-green interactions were enhanced.

Two clusters that were grown without torsions for the BCI 5P system are illustrated in Fig. S4. In both examples, the lack of torsions allows the blue particles to form alternative crystalline forms that only incorporate a relatively small number of icosahedral clusters. In Fig. S4a the blue particles form a BC8 crystal. In Fig. S4b the blue particles form a distorted hexagonal diamond crystal where patches 1–3 form the bonds within the hexagonal layers, and patch 4 the interlayer bonds. In both cases, orientational coherence is lost between the crystalline matrix and incorporated icosahedral clusters (see the bottom panel of Fig. S4c).

Interestingly, the dihedral angle distributions for the blue-blue bonds in the BC8 case are very similar to those in the BCI QC. This is consistent with the features of the blue particles noted in the previous section.

In the BCI 2P-mod system, one of the modifications is to restrict patch 4 of the blue particles to only bind to the relevant patch on the green particles and not to itself (Table S8). This change hence prevents the system being able to form a BC8 crystal purely from blue particles, and hinders phase separation more generally. For this reason, we also tested whether the BCI 2P-mod system might be able to form a quasicrystal when the torsional interactions were turned off. In this case, an IQC was still able to form, due to the lack of competing crystalline forms.

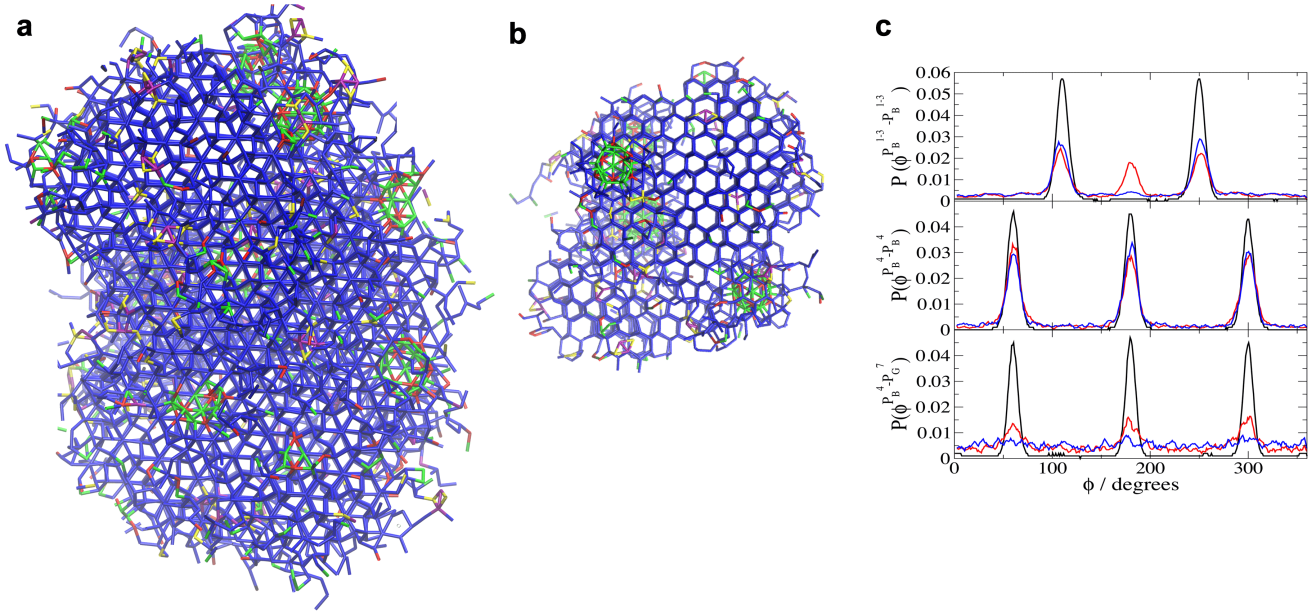

FIG. S4. **a** and **b**, Two examples of clusters grown with the BCI 5P model without torsion contributions to the energy. In both examples triacontahedra clusters form successfully, but blue particles tend to phase separate, forming small crystals, such as BC8 in **a** and a stacking of hexagonal layers (somewhat deformed to adapt to the blue particles' deviations from regular tetrahedral geometry) in **b**. These results strongly suggest that torsional interactions are required when the particles can form alternative ordered structures. **c**, Probability distribution of the dihedral angles in bonds formed by blue particles in the clusters **a** (blue line) and **b** (red line), as compared to those for the IQC formed with the BCI 5P model (black line). $P_B^4 - P_G^7$ bonds exhibit quite flat distributions that evidence that the blue particles are not able to bind with the right orientation to green particles in the triacontahedral clusters. Whereas the cluster shown in **a** exhibits dihedral distributions for the blue-blue bonds that are very similar to those of the IQC obtained with the BCI 5P model (albeit with somewhat less sharp peaks), the **b** cluster exhibits an extra peak for the $P_B^{1-3} - P_B^{1-3}$ bonds.

The main difference in the PI models that allows them to form QCs without a torsional component to the potential is the binary nature of the matrix—as there is no particle for which all patches can be self-interacting, any competing crystalline structure would have to be more complex than the BC8 crystal seen for the BCI systems and involve at least two types of particles. There must be sufficient specificity in the patchy interactions of the blue and green particles that precludes alternative crystalline forms even in the absence of torsions. Similar behaviour has been seen before in

crystal-forming patchy-particle models.[2] A ternary clathrate-forming model was still able to form the target crystal in the absence of torsions, but the removal of the torsions caused the BC8 model to also form hexagonal diamond crystallites. Similarly, a recent paper introduced a scheme to design patchy particle systems (without torsions) to stabilize a target crystal by systematically increasing the specificity (including by introducing new particles types) until only the target structure could assemble.[3]

D. Effects of patch width

The effects of the patch width parameter have been considered in previous simulations of patchy-particle self-assembly with variants of the current potential.[4–6] Where the patch vector geometry exactly matches a target structure, as is the case here, the target structure remains the favoured ordered form as the patch width is decreased. The main effects of reducing the patch width are instead to reduce the kinetic accessibility of the target state and to reduce the temperature at which it becomes stable with respect to a low-density fluid (the narrower patches mean condensed states have less vibrational entropy). As the patch width increases, the directionality of the interactions becomes less pronounced, and hence, at a certain point, there will generally be a crossover to the structures favoured by a more close to isotropic potential. When the patch geometry does not perfectly match any target structure, the dependence of assembly behaviour on the patch width can be more complex. For example, this is the case for the two-dimensional patchy particles with five regularly spaced patches that form a dodecagonal quasicrystal for a limited range of patch width and temperature. In this system, the crystalline ground state changes from one which has five imperfectly-oriented bonds to one that has three perfectly-oriented bonds as the patch width decreases.[7,8]

In the results reported so far, we have used an intermediate value of the patch width, namely $\sigma_{\mathrm{ang}} = 0.3$, where the patches are sufficiently narrow to favour the target structure, but whilst being wide enough to retain reasonable assembly kinetics. We expect the preference for IQC formation to be unchanged by narrowing the patch width and to continue until the potential becomes insufficiently directional as the patch width increases. We checked that this scenario holds by running simulations for the PI 3P NT system at different patch widths. At $\sigma_{\mathrm{ang}} = 0.15$ IQC formation still occurs albeit with a significantly smaller growth rate. Similarly, at $\sigma_{\mathrm{ang}} = 0.5$ an IQC is also able to assemble. However, at $\sigma_{\mathrm{ang}} = 0.6$ the assembled structure no longer exhibited any global orientational order.

E. Indexing diffraction patterns

The peaks in the diffraction pattern can be assigned using basis vectors along the six five-fold symmetry axes of a regular icosahedron; i.e.

$$\mathbf{Q} = a^* \sum_{i=1}^{6} n_i \mathbf{b}_i, \tag{S1}$$

where

$$\mathbf{b_1} = (1, \tau, 0) \qquad \mathbf{b_2} = (\tau, 0, 1) \tag{S2}$$
$$\mathbf{b_3} = (0, 1, \tau) \qquad \mathbf{b_4} = (-1, \tau, 0) \tag{S3}$$
$$\mathbf{b_5} = (\tau, 0, -1) \qquad \mathbf{b_6} = (0, -1, \tau). \tag{S4}$$

This basis corresponds to the icosahedron being oriented with two-fold axes along x, y and z. The set of six integers $(n_1 n_2 n_3 n_4 n_5 n_6)$ then uniquely identifies a peak.

An alternative scheme is to use basis vectors along x, y and z, but of two lengths (1 and τ); i.e.

$$\mathbf{Q} = a^*(h + h'\tau, k + k'\tau, l + l'\tau). \tag{S5}$$

In this scheme, peaks are labelled using the notation $(h/h'\, k/k'\, l/l')$. The relationship between the two sets of indices is that

$$2n_1 = h + k' \qquad 2n_4 = -h + k' \tag{S6}$$
$$2n_2 = l + h' \qquad 2n_5 = -l + h' \tag{S7}$$
$$2n_3 = k + l' \qquad 2n_6 = -k + l'. \tag{S8}$$

As the n_i must be integers, the above equations place restrictions on the possible values of h, h', k, k', l, l'.

All such **Q** vectors can potentially give rise to peaks in the diffraction pattern for a primitive IQC (although the intensity for most will be too small to be observed). By contrast, for body-centred and face-centred icosahedral (FCI) QCs only a subset of these **Q** are allowed. For BCI those for which $h+k+l$ (or equivalently $h'+k'+l'$ or $\sum_i n_i$) is even are allowed. And for a FCI QC, all indices must be even, and $h+l+h'+k'$ and $h+k+l'+k'$ (and $l+k+h'+l'$) must be a multiple of 4. These differences can help to identify an IQC as primitive, body-centred and face-centred based on their diffraction patterns. The patterns along the two-fold axis display the most obvious differences.

As well as the above, indexing the diffraction patterns is aided by computing

$$\mathbf{Q}_{\mathrm{perp}} = (h' - h\tau)\mathbf{i} + (k' - k\tau)\mathbf{j} + (l' - l\tau)\mathbf{k} \tag{S9}$$

for possible Bragg peaks, as the intensity is expected to be greatest for those with small Q_{perp}.

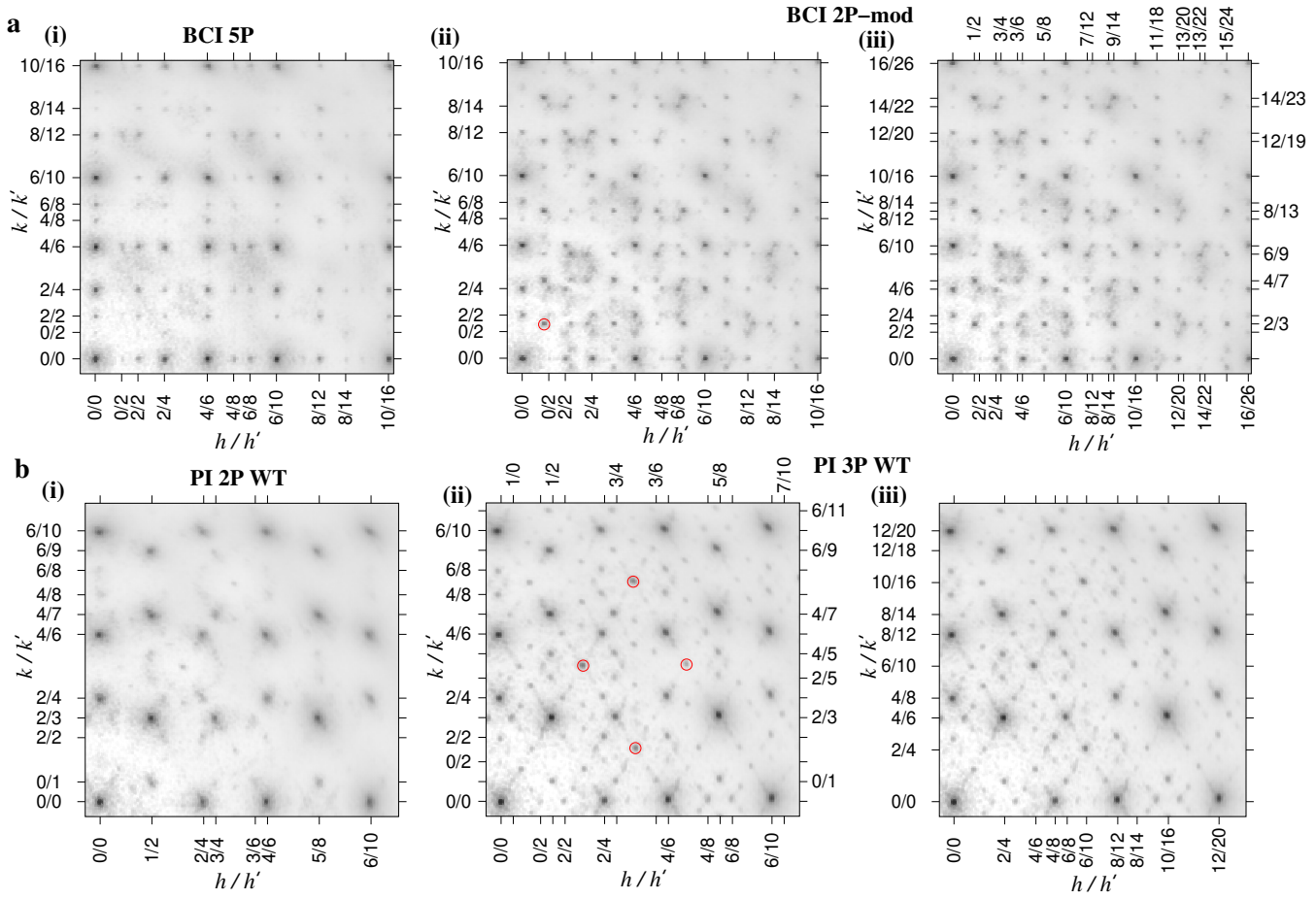

FIG. S5. Indexing of the positive quadrant of the two-fold diffraction patterns for example **a** BCI and **b** PI systems. The x and y axes are labelled with the h/h' and k/k' values that index the peaks ($l/l' = 0/0$). **a(i)**, A BCI indexing scheme can account for all the peaks in the BCI 5P system. **a(ii)**, However, when this scheme is applied to the BCI 2P-mod system, there are additional peaks that satisfy the BCI extinction condition—one is highlighted. **a(iii)**, Instead, all the peaks can be accounted for using a primitive indexing with $a_{\mathrm{PI}} = \tau a_{\mathrm{BCI}}$. **b(i)**, A primitive indexing scheme well describes the PI 2P WT system. **b(ii)**, The PI 3P WT has a more well-resolved diffraction pattern, and although the primitive indexing scheme can account for the most intense and many of the weaker peaks, peaks such as those highlighted are not explained. **b(iii)**, Instead, a FCI indexing scheme with $a_{\mathrm{FCI}} = 2a_{\mathrm{PI}}$ enables the pattern to be fully indexed.

In Fig. S5a(i) we show an indexed two-fold diffraction pattern for the BCI 5P system for the $+x/+y$ quadrant. We use the $(h/h'\,k/k'\,l/l')$ notation. All peaks in the BCI pattern satisfy $h'+k'+l'$ is even. Together with the pattern's similarity to that for the ideal BCI QC (Extended Data Fig. 2), this provides strong evidence that this system indeed has BCI character.

The diffraction pattern for the BCI 2P-mod system is more complex. Although the most intense peaks are the same as for the BCI 5P system, there are additional weaker peaks that cannot be indexed using the BCI indexing scheme. For example, in this scheme the highlighted peak in Fig. S5a(ii) would be indexed as (1/1 1/2 0/0) but this

would lead to non-integer n_i. However, these peaks can be satisfactorily indexed if a primitive indexing scheme is used with a scaling by τ, i.e. $a_{\mathrm{PI}} = \tau\, a_{\mathrm{BCI}}$ (Fig. S5a(iii)), where a is the hypercubic lattice parameter. For example, the highlighted peak now occurs at (1/2 2/3 0/0).

The diffraction pattern for the PI 2P WT system is shown in Fig. S5b(i). This can be satisfactorily indexed assuming a primitive hypercubic lattice. The most intense peaks include those that are common with the BCI pattern and have all even indices (e.g. (0/0 4/6 0/0)), as well as new peaks that have odd indices (e.g. (1/2 2/3 0/0)). These intense peaks are characteristic of a primitive IQC (see, for example, the diffraction pattern for the ideal primitive IQC in Extended Data Fig. 5).

The PI 3P WT diffraction pattern shown in Fig. S5b(ii) is similar to that for PI 2P WT. The most intense peaks are the same, but, as it is more well resolved, there are a greater number of weak Bragg peaks. Many of these are consistent with the primitive indexing scheme used for PI 2P WT. However, there are a number of weaker peaks that do not fit with this scheme. The most prominent of these are the highlighted peaks that form a diamond (e.g. (3/5 1/2 0/0) that are not allowed for a primitive IQC because they lead to some n_i values being half-integer.

This led us to also consider an FCI indexing of the pattern in Fig. S5b(iii) with a hypercubic lattice parameter that is twice that for the primitive scheme. This allows all the peaks to now be indexed. However, the intensity pattern of the peaks is not typical of a face-centred IQC. Rather, the pattern looks more typical of a PI pattern but with the addition of some lower intensity peaks typical of a face-centred IQC. Similar behaviour has been seen in experimental IQCs. For example, the AlPdMn system exhibits IQCs that switch from PI to FCI character as the Pd content is increased.[9] This happens by the appearance of additional FCI peaks which grow more intense as the Pd content is increased until a archetypal FCI pattern is observed. This transition occurs due to superstructural ordering of the primitive lattice due to greater chemical ordering.

What the nature of the superstructural ordering is in the PI 3P systems that leads to the appearance of the FCI peaks is not fully clear. Interestingly, in the absence of the red particles, i.e. in the PI 2P systems, there is little sign of this ordering (although this might in part be due to the diffraction patterns being not as sharp) and, as already noted, the diffraction patterns are consistent with a PI description.

F. Coordination number analysis

The coordination number distributions in the BCI and PI models are given in Fig. S6 using two methods to compute the coordination number. The first approach defines neighbours by a simple radial cutoff, where we use distance cutoffs that are similar to those used for the environment analysis of the ideal QCs. The second approach defines neighbours as a particles that share a patch-patch bond. The distributions resulting from the two approaches are generally very similar, but, for example, in some instances there will be particles which are close enough to be deemed neighbours by being within the distance cutoff, but which do not share a patch-patch bond.

For all the BCI systems, by far the most common coordination number is four. The proportion with a coordination number of four is highest for the BCI 2P system because both particle types have four patches. One noticeable feature is that the approximant and the BCI 5P and 3P systems have a significantly larger proportion of particles with coordination numbers of 6 or 7 than the ideal BCI QC, because of the greater tendency to form perfect triacontahedra (note that the disappearance of the peak at a coordination number of 7 for the BCI 3P system in Fig. S6c is simply due to the removal of the patches mediating green-green interactions in the triacontahedra). The patchy particle systems also all have a greater proportion of particles with a coordination number of three, and this is mainly a consequence of the greater likelihood of the blue particles having one missing bond (Extended Data Fig. 6d).

The BCI QCs have very similar coordination number distributions to those BCI QCs observed in the low-density regime of Ref. 10 with the proportion of 6- and 7-coordinate particles lying between that for the ideal BCI QC and the BCI 5P and 3P systems. In addition, in their intermediate-density regime icosahedral clusters equivalent to those highlighted in Fig. 1d become increasingly prevalent. This similarity is not surprising given that the higher-dimensional structural model obtained for the IQC in Ref. 10 is very similar to that used to generate our ideal BCI QC.

The coordination number distributions for the ideal PI QC and its 8/5 approximant have significant differences from the simulated PI systems. Firstly, their average coordination numbers are larger; this is also reflected in their higher density (Extended Data Fig. 7b). This partly reflects that only a subset of the environments present in the ideal PI QC and its approximant are represented by the patchy particles. For example, the 6-coordinate environment 5 (Table S2) is the most numerous in the ideal PI QC, but is one of those not represented. Consequently, the proportion of particles with coordination number 6 is much higher in the ideal PI QC and the 8/5 approximant. Also, that significant numbers of the patchy particles are not fully bonded leads to a much greater proportion of particles with coordination number of 4 or fewer. The lower average coordination numbers and density for the PI 2P systems is a simple consequence of the reduced average number of patches per particle.

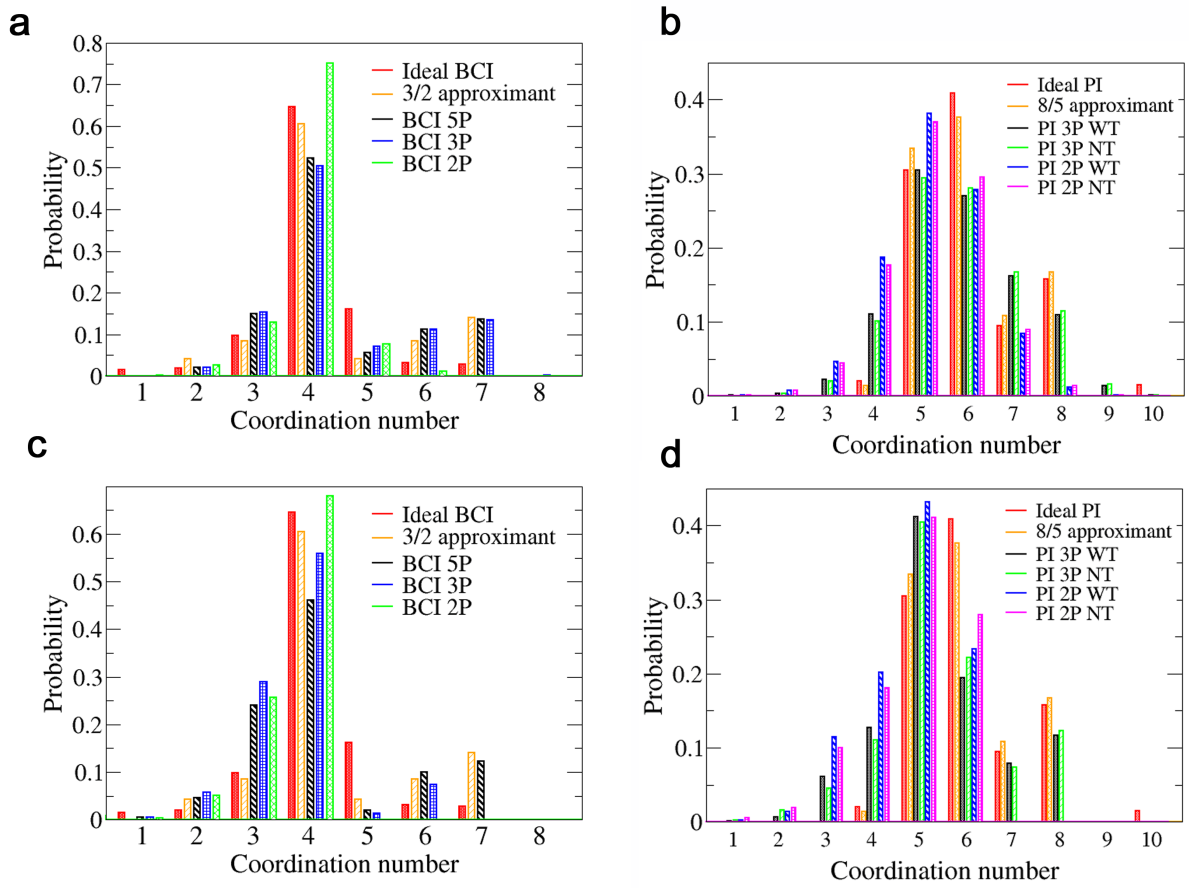

FIG. S6. Coordination numbers in the simulated IQCs based on the **a** and **c** ideal BCI and **b** and **d** ideal PI QC models. For comparison, data for the ideal IQC as well as their approximants are also included. In **a** and **b** coordination numbers were calculated counting the neighbours within a distance of $1.4\,\sigma$ for the BCI (corresponding to the first minimum in the PDF) and within $1.22\,\sigma$ for the PI (corresponding to the second minimum in the PDF). In **c** and **d** coordination numbers for the patchy particle systems were calculated by counting the number of patch-patch bonds. For the BCI 5P model, both conventions give very similar coordination-number distributions. Note that these distributions are similar to those of the low density IQC found in Refs. 10 and 11. The BCI 3P and BCI 2P models exhibit a lower coordination, especially when the actual number of patch-patch bonds is considered. In these cases, the coordination number is limited by the maximum number of patches on a particle, i.e. to six in the BCI 3P model and to four in the BCI 2P model. The coordination numbers in the PI QCs are larger than those in the BCI QCs. Coordination numbers are limited to a maximum value of eight in the PI 3P models and to six in the PI 2P models when evaluated counting the patch-patch bonds.

Given the differences in the average coordination number depending on the criteria used to define neighbours, we have also calculated the contributions to the BOODs using both approaches. The BOODs calculated using a distance cutoff (Fig. S7) exhibit more spots than the BOODs calculated using the patch-patch bonds (Extended Data Fig. 8) albeit still always oriented along either the five-, three- or two-fold axes. Thus, even when non-bonded particles are taken into account, the first coordination shells in these systems still exhibit very clear local icosahedral symmetry.

	⟨CN⟩	
System	cutoff	patch-patch
ideal BCI	4.13	
3/2 approximant	4.64	
BCI 5P	4.50	4.23
BCI 3P	4.50	3.74
BCI 2P	3.91	3.60
BCI 2P-mod	3.98	3.68
ideal PI	6.12	
8/5 approximant	6.08	
PI 3P WT	5.81	5.41
PI 3P NT	5.88	5.47
PI 2P WT	5.18	4.75
PI 2P NT	5.22	4.80

TABLE S10. Average coordination number (CN) for the ideal IQC, their approximants and the simulated IQCs. The values are calculated either using a distance cutoff or the number of patch-patch bonds in the same way as in Fig. S6.

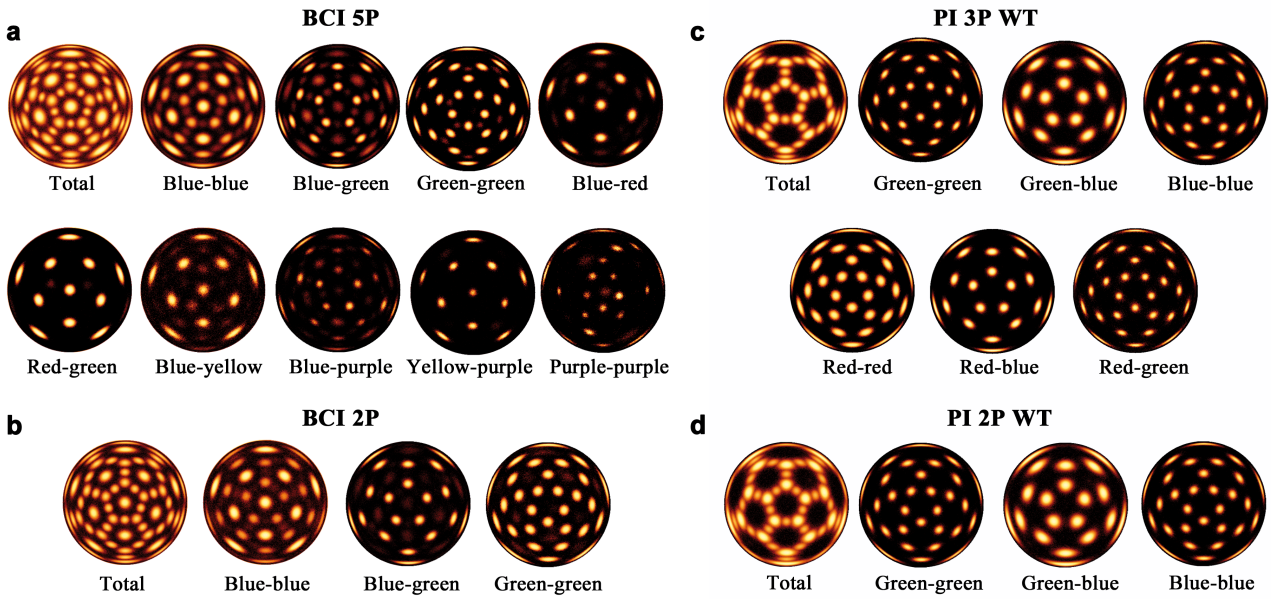

FIG. S7. Contribution to the BOOD for the **a**, BCI 5P and **b**, BCI 2P and **c**, PI 3P WT and **d**, PI 2P WT QCs from the different pairs of nearest neighbours defined as those within a distance cutoff of $1.4\,\sigma$ for the BCI and $1.22\,\sigma$ for the PI. Different from the contributions shown in Extended Data Fig. 8a–d, additional spots can occur in directions not expected from the geometry of the particles (Extended Data Fig. 8e,f) due to non-bonded neighbours. For example, for the BCI systems there are weak additional spots in the blue-blue, blue-green, green-green and blue-purple BOODs. For the PI systems, even though there are no blue-blue, green-green and red-green patchy interactions, the corresponding BOODs have spots directed along two-fold axes associated with non-bonded nearest neighbours pairs.

S4. DIRECT COEXISTENCE SIMULATIONS

A. Methods

Although our simulations have shown that the IQCs that we have discovered are strongly kinetically favoured, it would also be interesting to know whether they are also ever thermodynamically most stable. But to address this question we first need to know what the competing crystal forms might be. For the BCI 5P system, the particles can also form the 3/2 approximant shown in Fig. 1b. However, for the other patchy particle systems, the approximants to the IQCs are not known, as the particles are no longer able to represent all the environments present in the ideal IQCs (or their approximants). A potential route to identify the approximants in these cases would be to "lift" the observed IQCs into 6D and then project back to 3D with the obtained occupation domains oriented so as to produce an approximant.

As the IQCs are expected to have a greater entropy than any periodic approximants, if the IQCs are ever the most stable phase, this would be expected to be in a region of the phase diagram bounded at high temperature by their melting; thus, IQC stability would be indicated by the IQC having a higher melting point than the approximant.

To probe the relative stability of the BCI quasicrystal and its 3/2 approximant for the BCI 5P system, we attempted to estimate their melting points using the direct coexistence approach.[12] In this approach a crystalline slab that spans the shorter dimensions of an elongated cuboidal simulation box is placed in contact with a fluid phase that fills the rest of the box. The key feature is that as the crystal grows or shrinks, the area of the crystal-fluid interface stays constant. Hence, if the crystal grows, the system is above the melting point of the crystal, whereas if the crystal shrinks the system is below the melting point. Thus, by studying the system at a series of temperatures, one can bracket the melting temperature. One practical difficulty is that the closer one is to the melting point, the slower the net diffusive motion of the interface becomes. In Ref. 8 it was suggested that the direct coexistence approach could be extended to quasicrystals, for which direct calculation of their free energy by approaches such as thermodynamic integration are hindered by a lack of an appropriate reference state. The one additional difficulty is generating a quasicrystalline slab that spans the periodic boundary conditions without substantial defects given that the quasicrystal has symmetries that are incompatible with translational periodicity.

For the 3/2 approximant, the starting configuration of the system contains 18 176 particles ($284 \times 4 \times 4 \times 4$) in the crystalline slab and 6684 particles in the fluid phase. The slab configuration is an approximant crystal structure with 4 unit cells along each dimension. The fluid phase has the same composition as the solid phase, but the particles are randomly placed in the simulation box. Both phases are equilibrated at constant NPT, with $p^* = P\sigma_{\mathrm{LJ}}^3/\varepsilon_{\mathrm{LJ}} = 0.01$ and $T^* = 0.100$. After equilibration, the two phases are combined along the z-axis while avoiding overlaps at the interface. Then, the system is simulated at constant NPT, where only the z-length of the simulation box can change; $p^* = 0.01$ and $T^* = 0.090/0.100/0.105/0.107/0.110/0.112$.

For the quasicrystal, the starting configuration of the system contains 18 798 particles in the quasicrystalline slab and 13 202 particles in the fluid phase. The configuration is prepared by putting a quasicrystal seed with 8284 particles in a fluid of 23 716 particles with the same composition as the 3/2 approximant, and growing the seed across the periodic boundary of a cuboidal simulation box. The box length along z is longer than that along x and y in order to encourage the formation of a quasicrystal slab that is periodic across x and y. Because a quasicrystal is inherently aperiodic, it is difficult for it to merge with itself coherently across the periodic boundaries. To help mitigate this issue, the quasicrystal seed is oriented such that its two-fold symmetry axes are aligned with the x, y and z axes, but this may not entirely prevent grain boundaries from forming.

The growth simulation is performed at constant NVT, with $N = 32000$, $N/V^* = 0.5$ (where $V* = V/\sigma_{\mathrm{LJ}}^3$) and $T^* = 0.105$. After the slab is formed, it is equilibrated at constant NPT, with $p^* = 0.01$ and $T^* = 0.105$. The equilibration has two stages. In the first stage, only the x-length and y-length of the simulation box can change, while in the second stage, only the z-length can change. After equilibration, the system is simulated at constant NPT, where only the z-length of the simulation box can change; $p^* = 0.01$ and $T^* = 0.090/0.100/0.103/0.105/0.107/0.110$.

B. Results

Figure S8 and Figure S9 show the evolution of the system energy as a function of MC cycles for the 3/2 approximant and the quasicrystal slab, respectively. A common feature of the curves is their initial large slopes, but the curves gradually flatten out. This is due to further equilibration after the interface is set up, so only the slopes at the later stage of the simulations are meaningful.

For the approximant, the system energy reaches an approximately constant value at $T^* = 0.105$ and 0.107 but consistently increases at $T^* = 0.110$ or higher temperatures, and consistently decreases for $T^* = 0.100$ and below. Therefore, its melting point is certainly between 0.100 and 0.110, but it is hard to delimit it more closely. It is also

worth noting that the interface has a rather irregular shape, which is dominated by clusters formed by the red and green particles and less so by the blue particles in the matrix (Fig. S10). This is because of the greater stability of the interactions within the clusters than those within the matrix. The difference in stability could result in local free-energy barriers to growth because the growth of matrix is unfavourable while the growth of clusters is favourable. Such barriers are probably partly responsible for the slow dynamics associated with motion of the interface.

Similarly, the melting point of the quasicrystal slab is certainly between 0.107 and 0.090 (probably being above 0.100) but it is again hard to bracket it more precisely. Moreover, as described earlier, the preparation of the starting configuration could easily result in grain boundary formation. This is evident from its melting behaviour. Instead of uniform melting of the surface, melting proceeds along the grain boundary into the centre of the slab; this is partly evident from the snapshots in Fig. S11 but is very clear when visualizing configurations on screen. The grain boundary reduces the stability of the slab, and likely lowers its melting point.

Given the uncertainty in their melting points and the defective nature of the quasicrystalline slab, we cannot conclude whether the approximant is thermodynamically more stable than the quasicrystal. However, it is clear that they have similar stabilities. That the IQCs invariably form in our nucleation and growths simulation rather than periodic approximants shows that the IQCs are clearly kinetically favoured. This is likely related to the many more ways that growth can lead to the IQC than the periodic approximant.

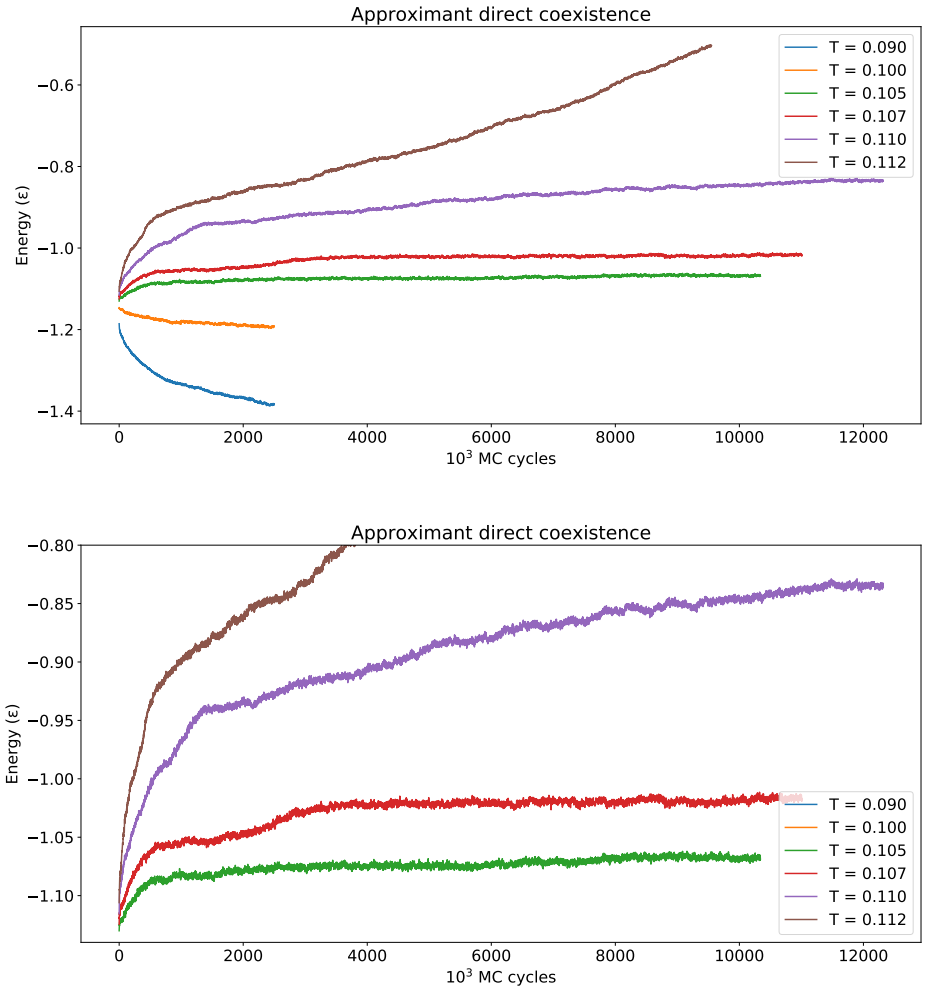

FIG. S8. Energy evolution in direct coexistence simulations of the 3/2 approximant. The bottom plot is an enlarged version of the top plot.

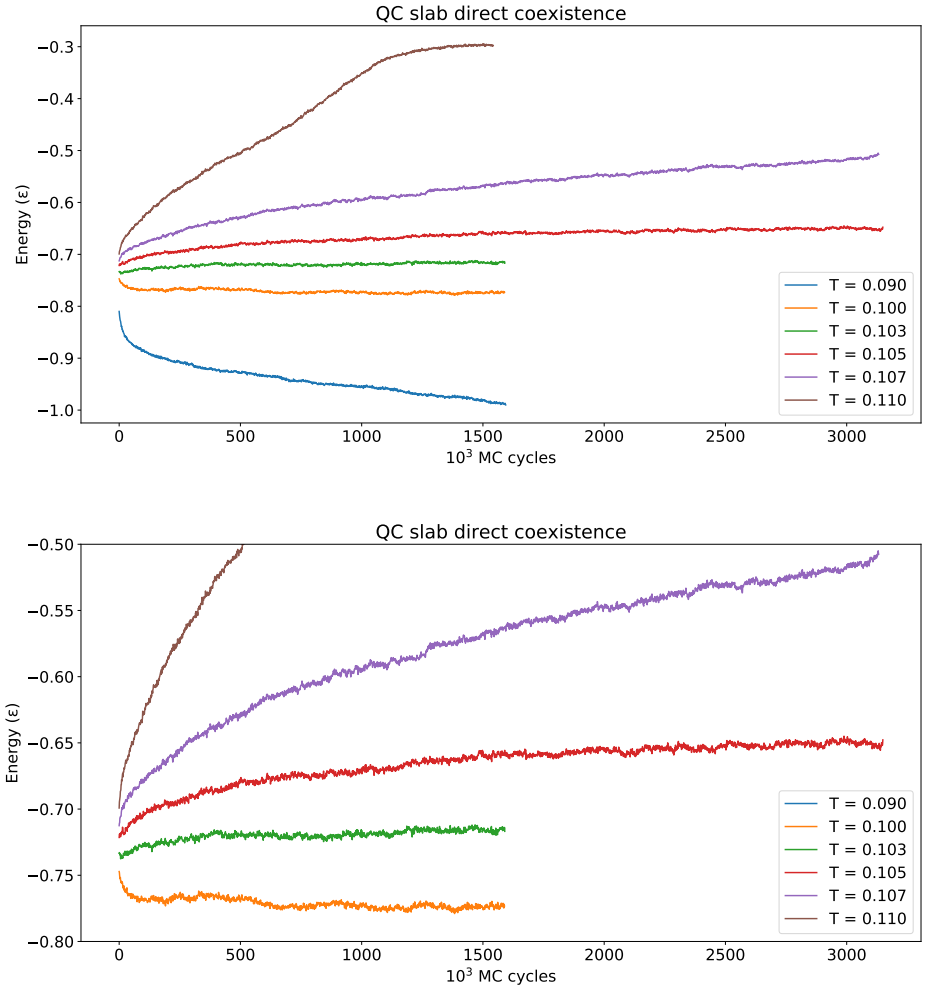

FIG. S9. Energy evolution in direct coexistence simulations of a quasicrystalline slab. The bottom plot is an enlarged version of the top plot.

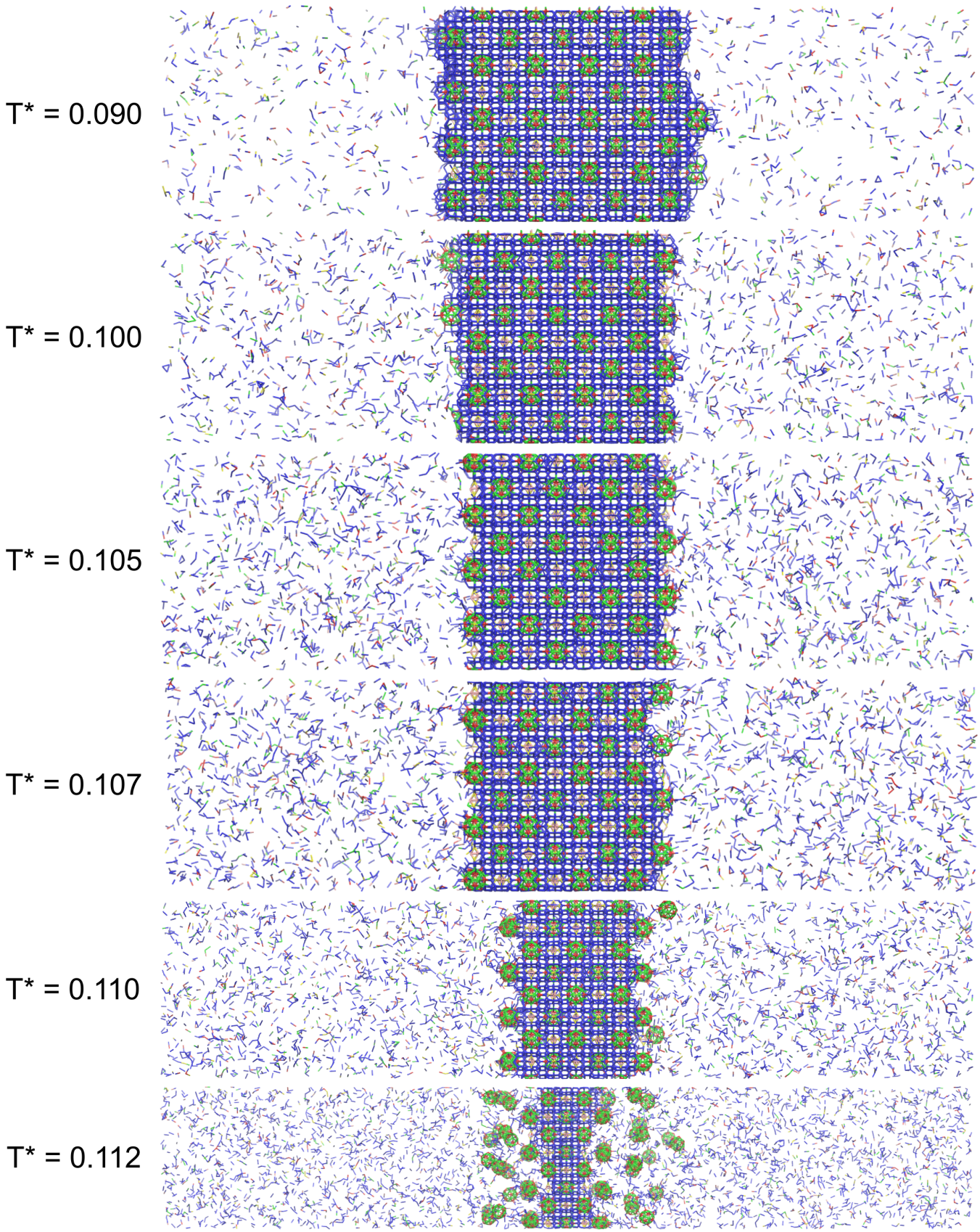

FIG. S10. Final configuration of direct coexistence simulations of the 3/2 approximant at various temperatures. The greater stability of the triacontahedral clusters than the blue matrix particles is evident both from their prominence at the surface, and their slower melting at higher temperatures.

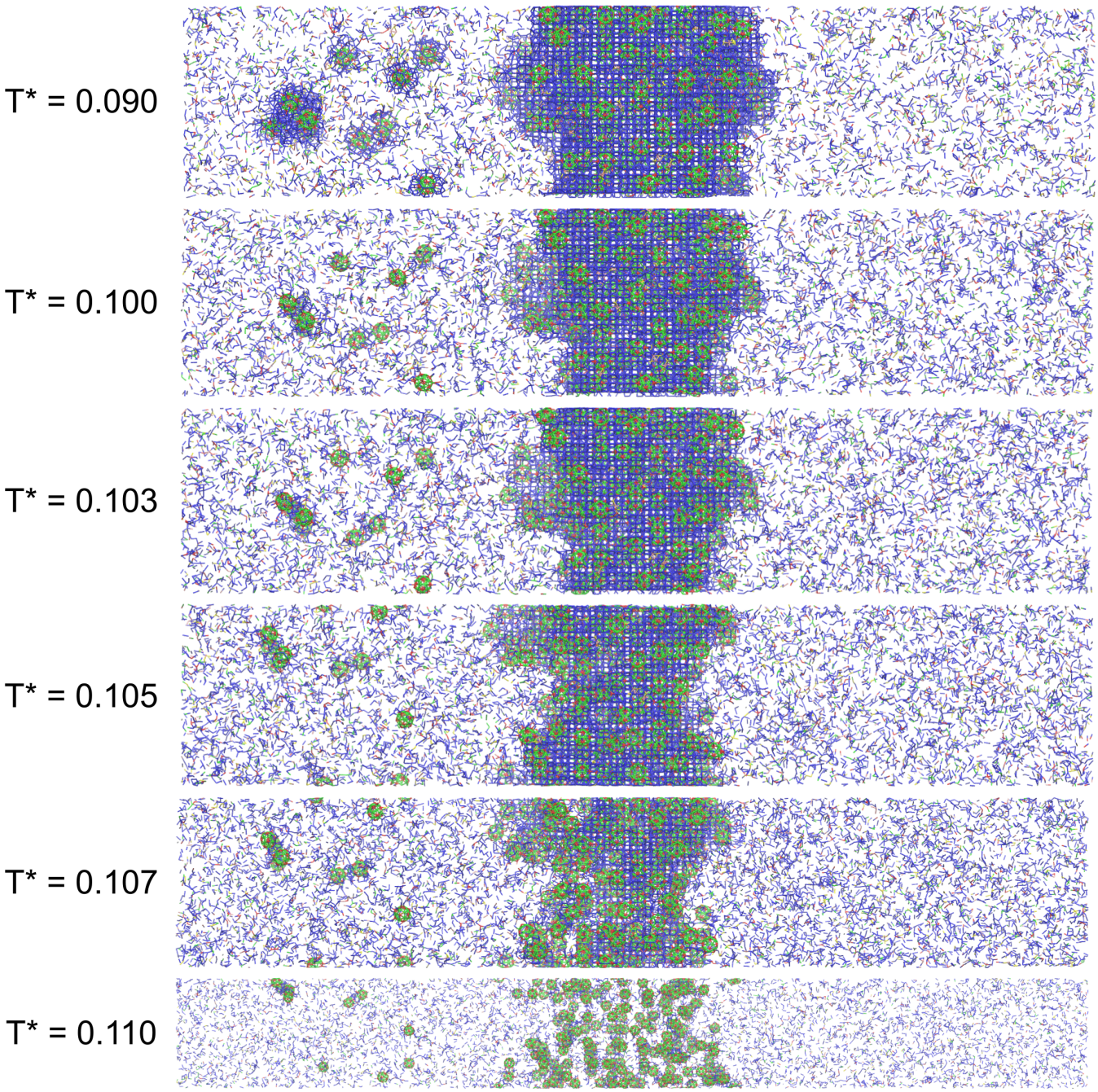

FIG. S11. Final configuration from direct coexistence simulations of a quasicrystalline slab at various temperatures.

S5. DNA ORIGAMI REALIZATION OF PATCHY PARTICLES

We focused on the realization of the most simplified patchy-particle design for the BCI QC. For each type of patchy particle, we generated a file in .ply format from the patch coordinates. Then, we converted the ply file to a DNA origami caDNAno design file using the TALOS program[13]. While running TALOS, we chose a minimum edge length of 63 base pairs, a flat vertex type, and a middle vertex connection layer. We used caDNAno[14] to add six-helix bundles to each vertex of the origami by extending the six outer helices at each vertex, two from each edge meeting at a particular vertex (Figure S12a). These extensions were modified with sticky ends to allow origamis to bind. The resulting caDNAno designs are shown in Figure S13 and Figure S14. Helices 0-35 compose the six edges of the tetrahedral wireframe, while helices 36-59 composes the four six-helix bundle extensions.

The torsional angles between bound origamis can be controlled by programming the strand sequence of the sticky ends. Using the simplified representation shown in Figure S12b, the designs that enable the three possible torsional angles are shown in Figure S12c. Letters A, B and C represent three different sets of sequences, where a letter with a plus sign is complementary to and binds to the same letter with a minus sign.

To illustrate in detail the realization of patchy particles as DNA origami, we chose the BCI QC patchy particles with two particles types (green and blue). We needed to modify the patch specificity and torsional angles because of the incompatibility between some patch specificity and torsional angles and the six-helix bundle extensions. In particular, P_B^4 can interact with itself, so it should be self-complementary. However, it also interacts with P_G^4, meaning that P_G^4 should have the same sequence as P_B^4 and also be self-complementary. However, P_G^4 does not interact with itself in the patchy particle design. Due to this apparent contradiction, we needed to remove the self-interaction of P_B^4. The other issue is related to the torsional angles of $P_B^{1,2,3}$. It is only possible to implement one or three, but not two, torsional angles using the scheme in Figure S12c. Since these patches have two possible torsional angles, it is not possible to implement it through the sticky ends, and so we needed to change it to three. The modified patchy particle designs are given in Table S8. We verified that the modified patchy particles (BCI 2P-mod) are still able to form an IQC in simulations. The sequence design of the sticky ends, which corresponds to the modified patchy particle design, is shown in Figure S12d.

After having designed DNA origami to represent each type of patchy particle, we assembled a cluster of DNA origami based on the cluster of patchy particles that serves as a fundamental building block of the BCI 2P quasicrystal. We first converted the caDNAno design file into oxDNA configuration and topology files using the tacoxDNA package[15]. Then, we placed and oriented the DNA origamis according to the patchy particle representation of the cluster. With the starting configuration prepared, we performed oxDNA[16,17] coarse-grained molecular dynamics simulation at 300 K with a Langevin thermostat and a time step of 0.005 simulation units, corresponding to 15 fs in real units. To speed up base pair formation between origami sticky ends, we applied harmonic mutual traps on pairs of sticky ends that should bind to each other. Once all the desired base pairs have formed, we removed the traps and equilibrated the cluster for 6×10^7 steps, equivalent to approximately 0.9 µs. The structure of the DNA origami cluster was stable over the entire simulation.

This procedure for representing a patchy particle using a DNA origami could potentially be generalized to patchy particles of a different shape and with a different number of patches, as long as they can be represented as a polyhedron. The torsional angles could also be fine-tuned by introducing twist into the six-helix bundle extensions. The inclusion of sections that remain single-stranded after two arms bind may also allow the torsional flexibility of the interactions to be tuned.

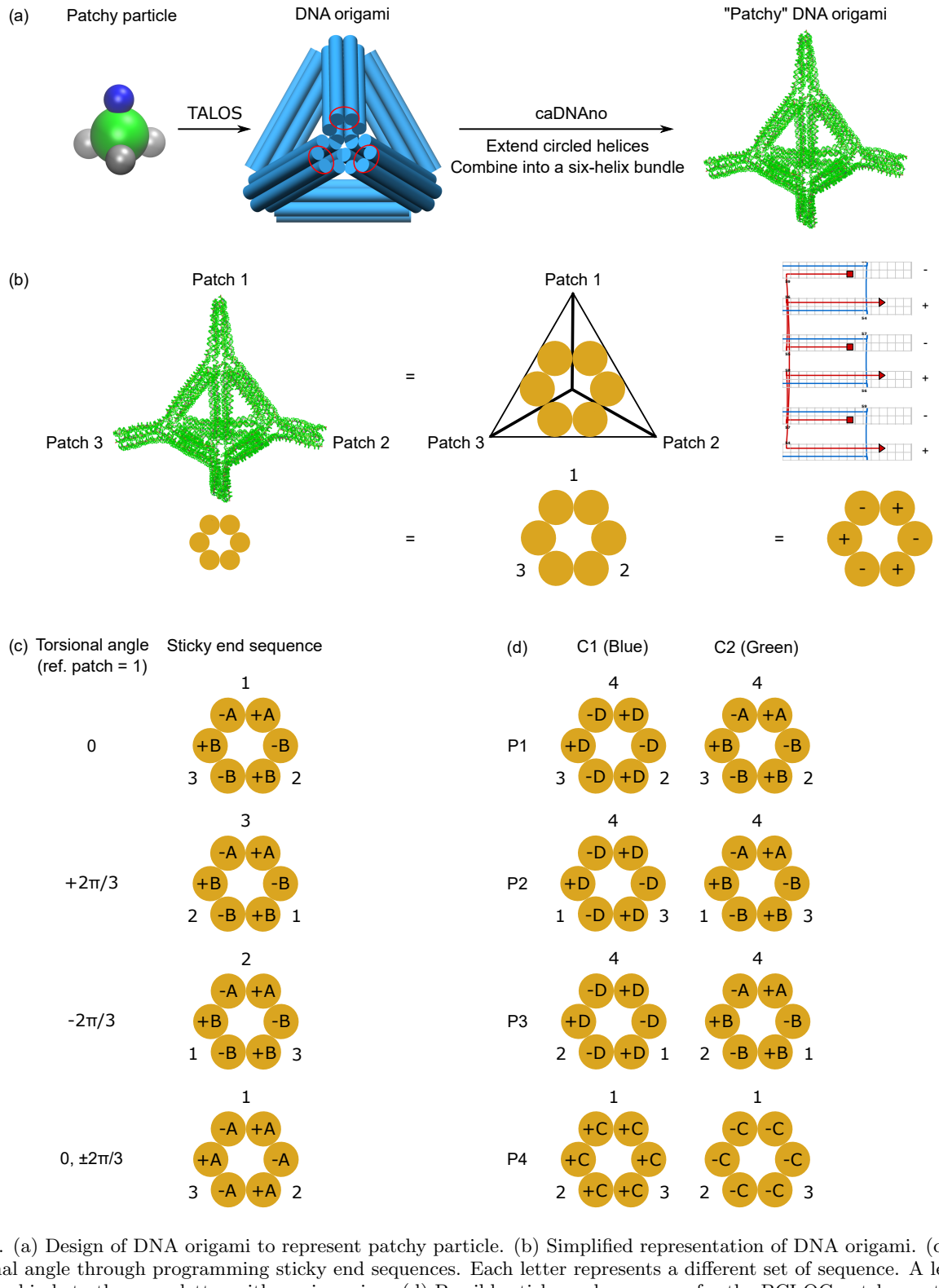

FIG. S12. (a) Design of DNA origami to represent patchy particle. (b) Simplified representation of DNA origami. (c) Control of torsional angle through programming sticky end sequences. Each letter represents a different set of sequence. A letter with a plus sign binds to the same letter with a minus sign. (d) Possible sticky end sequences for the BCI QC patchy particles with two particle types

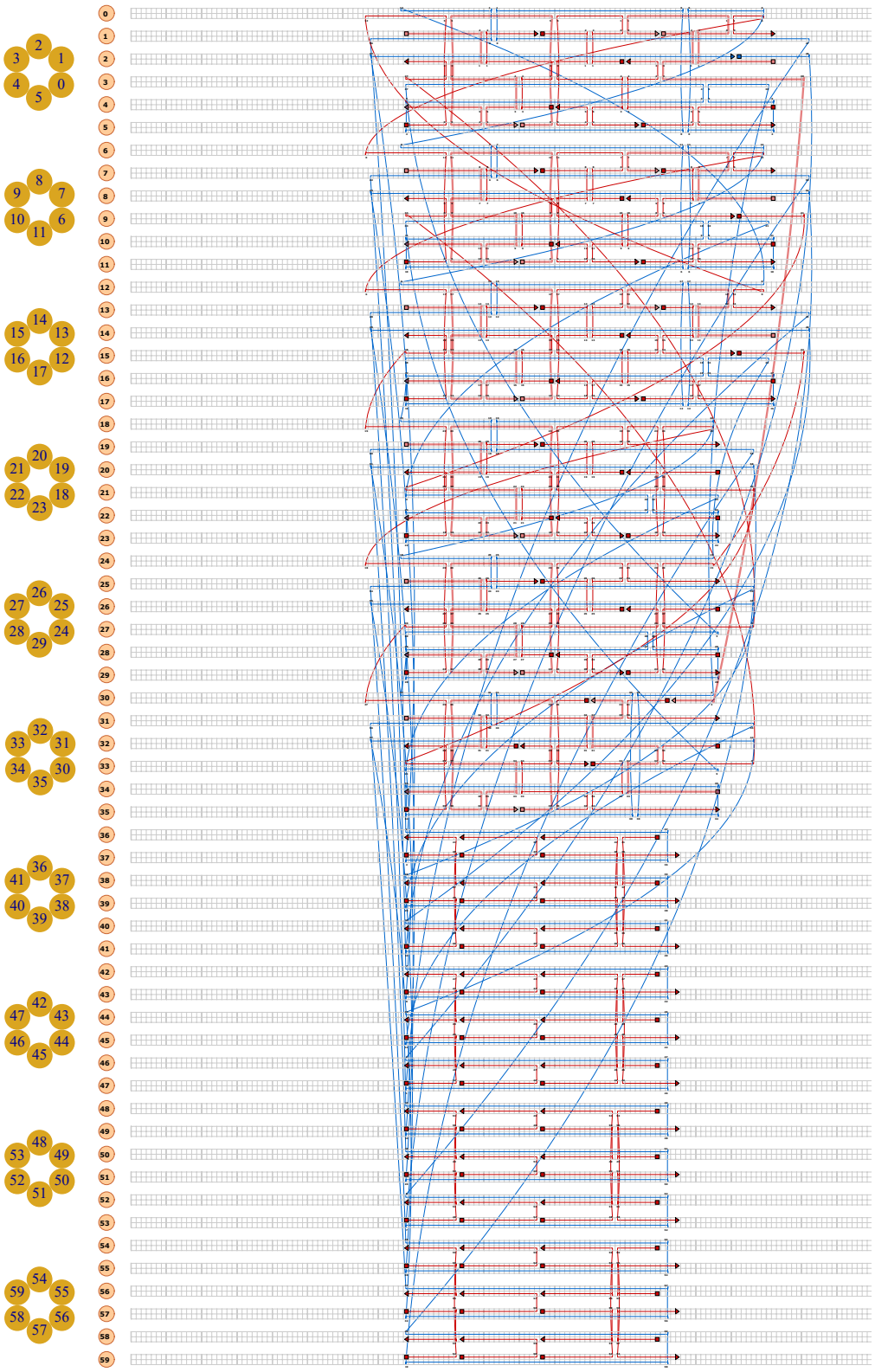

FIG. S13. caDNAno design for the DNA origami equivalent of the blue patchy particle.

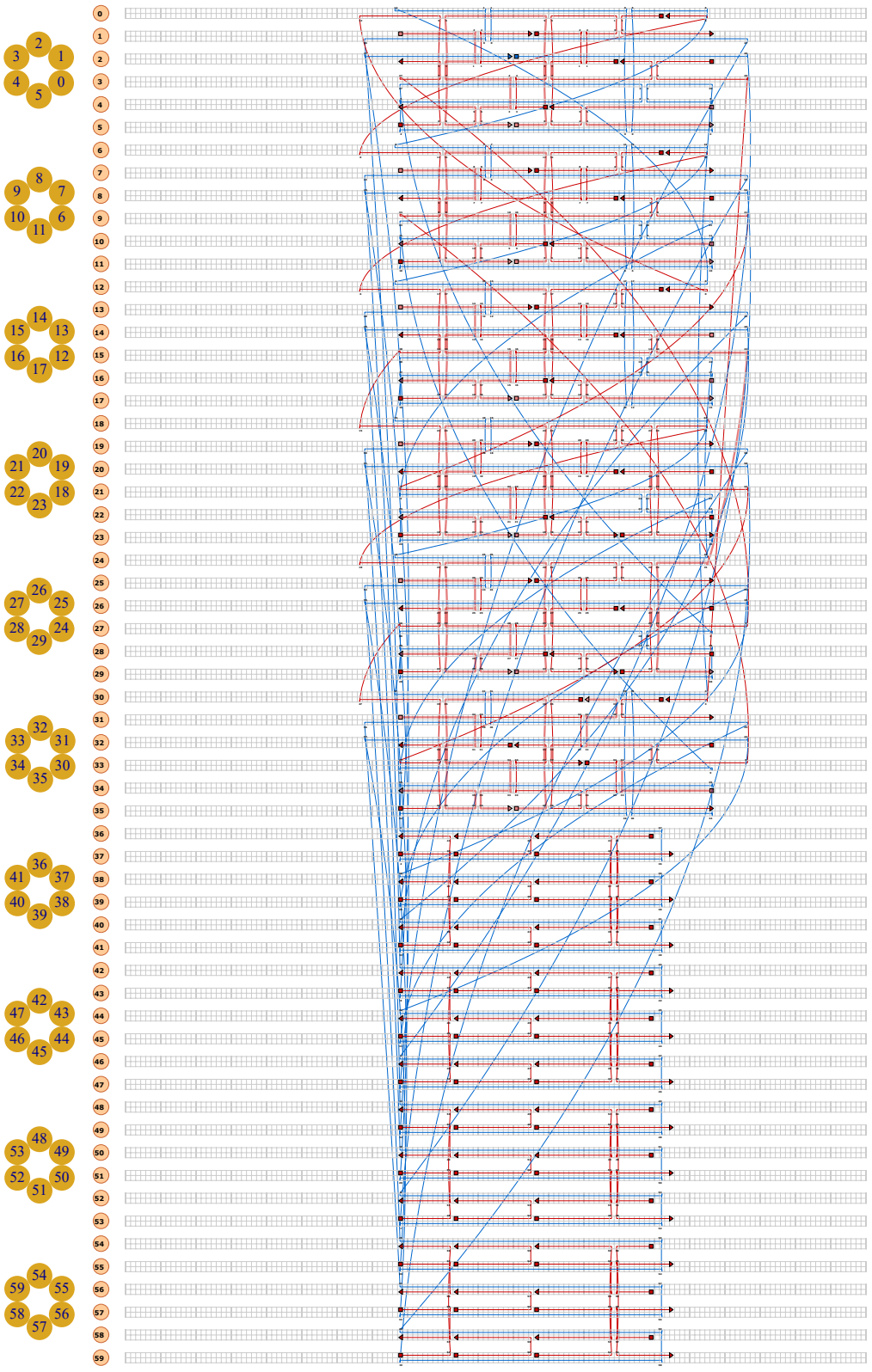

FIG. S14. caDNAno design for the DNA origami equivalent of the green patchy particle.

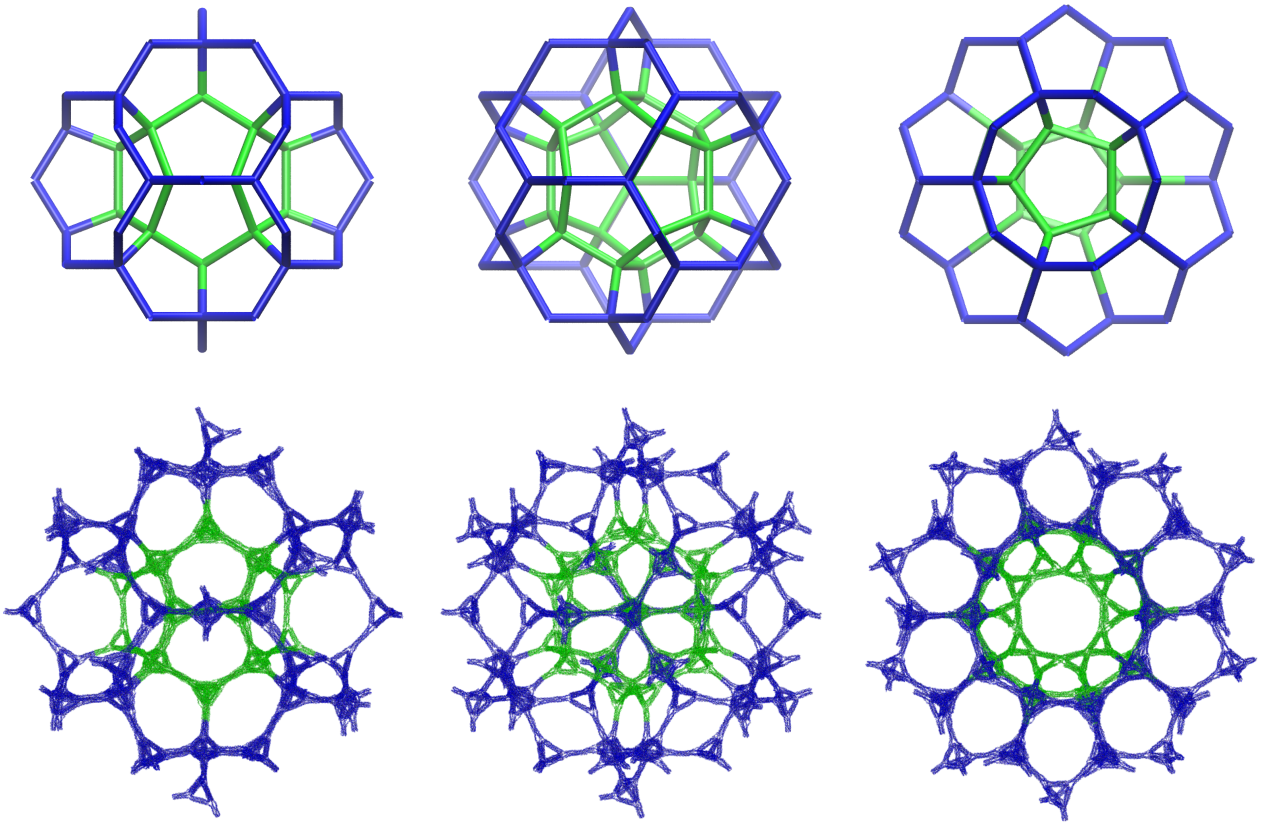

FIG. S15. Views of the assembled DNA origami cluster (bottom row) and their respective patchy particle representation (top row) along the two-, three- and five-fold axes.

REFERENCES

[1]Dmitrienko, V. & Kléman, M. Tetrahedral structures with icosahedral order and their relation to quasi-crystals. *Crystallogr. Rep.* **46**, 527–533 (2001).

[2]Tracey, D. F., Noya, E. G. & Doye, J. P. K. Programming patchy particles to form complex ordered structures. *J. Chem. Phys.* **151**, 224506 (2019).

[3]Romano, F., Russo, J., Kroc, L. & Šulc, P. Designing patchy interactions to self-assemble arbitrary structures. *Phys. Rev. Lett.* **125**, 118003 (2020).

[4]Wilber, A. W. *et al.* Reversible self-assembly of patchy particles into monodisperse icosahedral clusters. *J. Chem. Phys.* **127**, 085106 (2007).

[5]Wilber, A. W., Doye, J. P. K., Louis, A. A. & Lewis, A. C. F. Monodisperse self-assembly in a model with protein-like interactions. *J. Chem. Phys.* **131**, 175102 (2009).

[6]Wilber, A. W., Doye, J. P. K. & Louis, A. A. Self-assembly of monodisperse clusters: Dependence on target geometry. *J. Chem. Phys.* **131**, 175101 (2009).

[7]Doye, J. P. K. *et al.* Controlling crystallization and its absence: Proteins, colloids and patchy models. *Phys. Chem. Chem. Phys.* **9**, 2197–2205 (2007).

[8]Reinhardt, A., Romano, F. & Doye, J. P. K. Computing phase diagrams for a quasicrystal-forming patchy-particle system. *Phys. Rev. Lett.* **110**, 255503 (2013).

[9]Janot, C. *Quasicrystals. A primer* (Oxford University Press, Oxford, 2002).

[10]Engel, M., Damasceno, P. F., Phillips, C. L. & Glotzer, S. C. Computational self-assembly of a one-component icosahedral quasicrystal. *Nat. Mater.* **14**, 109–116 (2015).

[11]Damasceno, P. F., Glotzer, S. C. & Engel, M. Non-close-packed three-dimensional quasicrystals. *J. Phys: Condens. Matter* **29**, 234005 (2017).

[12]Vega, C., Sanz, E., Abascal, J. L. F. & Noya, E. G. Determination of phase diagrams via computer simulation: methodology and applications to water, electrolytes and proteins. *J. Phys.: Condens. Matter* **20**, 153101 (2008).

[13]Jun, H. *et al.* Automated sequence design of 3D polyhedral wireframe DNA origami with honeycomb edges. *ACS Nano* **13**, 2083–2093 (2019).

[14]Douglas, S. M. *et al.* Rapid prototyping of 3D DNA-origami shapes with caDNAno. *Nucleic Acids Res.* **37**, 5001–5006 (2009).

[15]Suma, A. *et al.* TacoxDNA: a user-friendly web server for simulations of complex DNA structures, from single strands to origami. *J. Comput. Chem.* **40**, 2586–2595 (2019).

[16]Ouldridge, T. E., Louis, A. A. & Doye, J. P. K. Structural, mechanical, and thermodynamic properties of a coarse-grained DNA model. *J. Chem. Phys.* **134**, 085101 (2011).

[17]Snodin, B. E. K. *et al.* Introducing improved structural properties and salt dependence into a coarse-grained model of DNA. *J. Chem. Phys.* **142**, 234901 (2015).